Remote Sensing of Environment 232 (2019) 111298

Contents lists available at ScienceDirect

Remote Sensing of Environment

journal homepage: www.elsevier.com/locate/rse

Multi-decade global gas flaring change inventoried using the ATSR-1, ATSR-2, AATSR and SLSTR data records

Daniel Fisher*, Martin J. Wooster

Kings College London, Geography Department, 40 Aldwych, London WC2B 4BG, UK
NERC National Centre for Earth Observation (NCEO), UK

ARTICLE INFO

Edited by Emilio Chuvieco

Keywords:
Industrial gas flaring
Thermal anomalies
Dataset
ATSR
SLSTR

ABSTRACT

The SWIR-radiance FRP method is applied to the Along Track Scanning Radiometer series of sensors, and the follow-on Sea and Land Surface Temperature Radiometer (SLSTR) sensor to provide both the longest and the most recent assessment of global gas flaring activity to date. Our inventory covers more than two decades, and demonstrates that total flare site numbers peak in 2008 (~14,000 global 1-arcminute grid cells containing flares) and that since then there has been an overall reduction to mid-2018 (~10,400 cells) When considering radiant heat output (SWIR-radiance derived FRP), a downward global trend identified between 2000 (~15.1 GW) and 2011 (~12.4 GW) has stalled, with a slight increase observed by mid-2018 (~13 GW). We also find through calibration against flared gas quantities derived from the Defence Meteorological Satellite Programme (DMSP) satellites, that ~131 billion cubic metres of natural gas has been flared globally between May 2017 and May 2018.

1. Introduction and background

Industrial gas flaring represents a source of air pollution that has regionally significant health impacts (Anenberg et al., 2012; Highwood and Kinnersley, 2006; Fawole et al., 2016; Anejionu et al., 2015b; Akpomuvie, 2011; Janssen et al., 2012). It is also a source of greenhouse gas (GHG) emissions, as well as being a waste of a valuable energy resource. At the global scale, gas flaring contributions to global GHG emissions are just < 2% of the nationally determined contribution targets defined as part of the Paris Climate Agreement (Elvidge et al., 2018). In relation to climate forcing, probably more significant is the fact that deposition of black carbon from flaring at higher latitudes can alter polar albedo, with climate feedbacks that are global in scale (Bond et al., 2013; Doherty et al., 2010; Flanner et al., 2007; Hadley and Kirchstetter, 2012; Huang et al., 2015; Ramanathan and Carmichael, 2008; Serreze and Barry, 2011; Stohl et al., 2013). Given these adverse environmental effects, reductions in global gas flaring have been called for, and are supported by various intergovernmental initiatives (The World Bank, 2015, 2011). Determining the success or failure of such reduction initiatives is dependent on effective long-term monitoring, and this process is now heavily reliant on satellite Earth Observation (EO) approaches that can provide regular, low-cost and reliable observations of flaring activities, and are gradually replacing in-situ or usage-estimation based approaches that have significant variability in their consistency (Ismail and Umukoro, 2012). Whilst the potential for EO based monitoring of gas flaring activity was established in the 1970s (Croft, 1973), and various detection and characterisation algorithms have since been proposed (Anejionu et al., 2014, 2015a; Casadio et al., 2012; Elvidge et al., 2013; Chowdhury et al., 2014; Elvidge et al., 2015; Muirhead and Cracknell, 1984; Faruolo et al., 2018, 2014), the first global, long-term EO-based gas flaring dataset is a relatively recent development, based on the low-light imaging capability of the Defence Meteorological Satellite Programme (DMSP) satellites' Operational Linescan System (OLS) (Elvidge et al., 2009). This method uses night-time OLS digital counts as an indicator of the intensity of flaring activity, and relates this to country level estimates of flared gas volumes (in billions of cubic meters, BCM) (Elvidge et al., 2009). Over the 15 years of OLS data examined (1994–2008), a strong correlation to gas flared volumes was found ($R^2 = 0.976$). More recently, the NightFire algorithm (Elvidge et al., 2015, 2013), using a Planck fitting approach applied to the night-time multispectral observations available from the Visible Infrared Imaging Radiometer Suite (VIIRS) imager operated on the Suomi-NPP satellite, has enabled the estimation of effective flaring temperature (K) and area (m^2) for gas flares, which via Stefan's Law can be used to produce estimates of their radiative power output (in W). This metric is well-established for the analysis of landscape fires, where it is referred to as Fire Radiative Power (FRP, Wooster et al., 2005, 2003), and is also useful for evaluating gas flaring activity since gas

---

* Corresponding author at: Kings College London, Geography Department, 40 Aldwych, London WC2B 4BG, UK.
E-mail addresses: daniel.fisher@kcl.ac.uk (D. Fisher), martin.wooster@kcl.ac.uk (M.J. Wooster).

https://doi.org/10.1016/j.rse.2019.111298
Received 18 January 2019; Received in revised form 27 June 2019; Accepted 2 July 2019

flare FRP is related to rates of methane consumption and carbon dioxide emission (Elvidge et al., 2015; Zhang et al., 2015).

Applied to VIIRS data from 2011 onwards, the NightFire approach has been used to generate BCM-based estimates of flaring activity from radiative power observations made at the scale of individual gas flares (Elvidge et al., 2015). An even longer-term assessment of global gas flaring is available from the Along Track Scanning Radiometer (ATSR) series of spaceborne sensors, which operated on the ERS and ENVISAT series of remote sensing satellites. A 19-year evaluation of ATSR night-time shortwave infrared (SWIR) data of persistent thermal anomalies produced country level estimates of flare counts as a proxy for flaring activity (Casadio et al., 2012). Whilst observable trends are evident with this approach, a significant limitation is that all flares are effectively assumed to be operating with parity, which is undermined by the observation that a significant proportion of flaring radiative power output arises from just a small subset of flaring sites (Elvidge et al., 2015). To better exploit the long-term ATSR dataset, and facilitate an absolute assessment of global gas flaring that takes this variability into account, Fisher and Wooster (2018) recently developed a single channel gas flare FRP estimation approach which can be applied to these sensors. Using single channel SWIR observations at night, and exploiting the near-constant ratio between the SWIR spectral radiance and total emitted radiance from emitters at gas flaring temperature ranges, estimates of gas flare FRP accurate to ± 13.6% are achieved (Fisher and Wooster, 2018). Here, we apply this SWIR-radiance method of FRP estimation to the entire three sensor ATSR time series, and to a year-long dataset collected by the latest instrument in the series, the Sea and Land Surface Temperature Radiometer (SLSTR). Our aim is to provide the longest assessment of global gas flaring produced to date, including quantitative calculations beyond simple gas flare counts.

2. Gridded gas flaring dataset generation from the ATSR and SLSTR data records

Besides industrial gas flaring, various other phenomena on the Earth's surface can attain combinations of kinetic temperature and spatial extent that produce sufficient signal to be observable in night-time SWIR imagery at moderate imaging resolutions (pixel resolutions of ~1 km). These phenomena include: biomass burning (Abuelgasim and Fraser, 2002; Casadio et al., 2012; Elvidge et al., 2013); active volcanoes (Wooster et al., 1998; Wooster and Rothery, 1997); and certain industrial activities unrelated to the flaring of gas (e.g. steel mills, power plants) (Elvidge et al., 2015; Liu et al., 2018). A further source is the South Atlantic Anomaly (SAA), which regularly results in randomly distributed pixels having raised SWIR signals not associated with any surface features (Casadio et al., 2012; Elvidge et al., 2015, 2013). Clearly, effective discrimination between the various causes of raised SWIR signals in night-time observations is required to accurately survey industrial gas flaring. Fortunately, such discrimination is mostly straightforward. Simple tests of 'hotspot' persistence for example typically enables most transient biomass burning activity to be discriminated from the far more temporally invariant industrial hotspots (Casadio et al., 2012; Elvidge et al., 2015; Faruolo et al., 2018). This section describes the various steps, summarised in the flow chart in Fig. S1, used to identify gas flaring activity in the ATSR and SLSTR datasets.

2.1. The along track scanning radiometer and the sea and land surface temperature radiometer

The ATSR and SLSTR sensors are two of a small number of spaceborne imaging radiometers that obtain SWIR imagery in the unilluminated part of the orbital node. The former's near 21-year time series is currently the longest night-time SWIR data record available. The ATSR sensor design features a dual view, conical-scanning geometry, though we focus on the 'nadir' view that scans the Earth across a 500 km swath using view zenith angles (VZA) ranging from 2° at the sub-satellite point to 22° at the edge of scan. Pixel area increases from ~1 to ~1.5 km^2 over this VZA range. The ATSR sensors were typically operated in a 35 day repeat cycle, providing revisits approximately every 5 days at the equator (Casadio et al., 2012). The first sensor in the series, ATSR-1, was launched in July 1991 on the ERS-1 satellite and operated through to May 1996. ATSR-2 operated on ERS-2 between April 1995 and December 2002, and the Advanced ATSR (AATSR) operated on Envisat between March 2002 and April 2012. Each ATSR showed excellent radiometric calibration (Smith et al., 2012; Smith and Cox, 2013) and in addition to the required SWIR channel (1.6 μm), all three also operated a midwave infrared (MWIR) channel (3.7 μm) which is used here to aid differentiation between thermal anomaly types (see Section 2.6.1). Unfortunately the ATSR-1 MWIR channel failed relatively soon after launch (May 1992), but to the benefit of this study resulted in the consistent and continuous capture of 1.6 μm SWIR observations at night (a switching day/night operation of these two channels was originally planned). Prior to the MWIR channel failure, the SWIR channel was only used to capture night-time data when the MWIR channel was near saturation (Wooster and Rothery, 2002), resulting in significantly reduced night-time SWIR sampling (see Fig. S2). Implications of the lack of MWIR observations for thermal anomaly differentiation in ATSR-1 data are discussed in Sections 2.6.1 and 2.6.2.

The first SLSTR sensor was launched on Sentinel-3A in February 2016. It shares the conical imaging design of its ATSR antecedents, albeit with major technical modifications to enable more spectral channels to be recorded and a far wider swath. In the non-symmetrical near nadir view, SLSTR scans over a 1407 km swath, with a maximum 60° VZA at the most oblique scan edge (and a 6° VZA at the sub-satellite point). SLSTR is operated in a 27 day repeat cycle, with revisits made every 1.9 days at the equator (Wooster et al., 2012). A second spacecraft, Sentinel-3B, launched in 2018 means daily coverage is now possible. SLSTR operates three SWIR channels, and here we use the 1.6 μm (S5) channel common to the ATSR sensors, as well as a new channel centred on 2.2 μm (S7) to aid discrimination between different persistent thermal anomaly types (see Section 2.6.1). SLSTR SWIR channels have a pixel size of 500 m at nadir, resulting in a ~×4 increase in sensitivity to sub-pixel thermal anomalies (Wooster et al., 2015), the implications of which are discussed in Section 2.3.

2.2. Data availability and time-series selection

All ATSR data used here are the 3rd reprocessing top-of-atmosphere (TOA) products taken from the Centre for Environmental Data Analysis (CEDA) archive. Data overlaps exist between ATSR-1 and ATSR-2 and between ATSR-2 and AATSR. Whilst using all available data is ideal, mechanical issues with ATSR-2 and its hosting ERS-2 satellite prevent this. From December 1995 through June 1996 the ATSR-2 sensor experienced a stall of the scan mirror, so only ATSR-1 data is used through this period until May 1996, with no ATSR coverage for June 1996. In January 2001 the ERS-2 satellite experienced a complete failure of the gyroscopic navigation system, with a suitable fix not being achieved until July 2001, resulting in ~6 months of missing ATSR-2 data. Given this, data from AATSR is used as soon as it becomes available in May 2002. The SLSTR data used in Section 4 are the most recent 12 months available on the CEDA archive at the time of this analysis (9th May 2017 through 8th May 2018). For validation activities undertaken in Section 3, SLSTR data of March 2017 was used.

2.3. Thermal anomaly identification

Various static and contextual threshold-based approaches exist for identifying thermal anomaly containing pixels (Casadio et al., 2012; Elvidge et al., 2015; Giglio et al., 2016; Roberts and Wooster, 2008; Schroeder et al., 2016, 2014; Zhang et al., 2017). However, for night-time SWIR observations simple static thresholds suffice as the absence of a solar reflected signal means the background signal consists only of instrument noise. All that is required to identify thermal anomaly pixels is the isolation of those pixels having signals above the instrument noise level:

$$G_x = \begin{cases} 1, & I_x \geq \eta \\ 0, & I_x < \eta \end{cases} \tag{1}$$

where x is any image pixel, G is a binary image of thermal anomaly locations, I is the input imagery and η is the sensor noise threshold. We undertook a simple evaluation of the noise behaviour of the AATSR 1.6 μm channel reflectance and obtained an η of 0.06, this value representing the extremes of the tails of the noise distribution and any SWIR signal above this should thus be associated with a thermal anomaly. To maintain consistency this same threshold was applied to both ATSR-2 and ATSR-1 night-time data, whilst for SLSTR it was increased by a factor of four to 0.24 (and converted from units of reflectance to spectral radiance) due to the four times smaller pixel area of the S5 (1.6 μm) nadir view data. It should also be noted that all SLSTR SWIR channel spectral radiances are adjusted by the scaling factors recommended in (Smith, 2018), which are 1.12 and 1.20 for S5 and S6 respectively, and that only pixels with VZA < 22° are considered to maintain consistency with ATSR and reduce effects introduced by increased oblique view angles and/or increased FOV overlap at more oblique viewing angles (Calle et al., 2009).

2.4. Persistent thermal anomaly gridded dataset generation

Thermal anomalies associated with volcanoes, industrial gas flares and other non-flaring industrial sites can all show strong temporal persistence at their locations, and this characteristic can be exploited to discriminate them from those related to transitory (i.e. biomass burning) and non-surface (i.e. SAA) phenomena. Temporal persistency testing follows a three stage process (Casadio et al., 2012; Elvidge et al., 2015):

1. A spatial aggregation of binary flagged swath data, G, to a 1-arcminute (~2 km) geographic grid.
2. A temporal aggregation of the re-gridded data to a monthly temporal scale, where one or more detections flags the grid cell for the month.
3. A persistence assessment is then made with a rolling twelve-sample window applied to the monthly gridded data. More concretely, a total of twelve twelve-sample assessments for flaring activity are made for each month, ensuring that all twelve-month periods intersecting with the month under evaluation are considered (for a more detailed explanation please refer to Section S1 of the Supplementary material). For ATSR data, any grid cell with at least four monthly thermal anomaly detections in any of the twelve-sample periods assessed is flagged as being persistent, and for SLSTR the requirement is reduced to two detections based on the significantly reduced number of twelve-sample periods available for consideration.

For the ATSR sensors, the rolling window is applied from August 1991 (ATSR-1 being active from this date) to April 2012 (AATSR failing with the loss of Envisat), and for SLSTR it is applied to all data from May 2017 to May 2018. Retaining the unique persistent detections, two 1-arcminute maps of persistent thermal anomaly locations are generated, one for the ATSR sensors and one for SLSTR.

The thermal anomaly sampling for the first and last 11 months of the ATSR time series is low biased, since not all 12 sample intersections are available for consideration for any given month, resulting in missed detection opportunities. For example, in the first month of the ATSR-1 time series only one twelve-sample intersection is available (the current month and the following 11 months). This is also a problem for the SLSTR dataset, as only one 12 sample intersection occurs for each month (as only 1 year is being evaluated in total). To limit the impact of this reduced opportunity for sampling at the edges of the time series, and to maximise potential flare detection in the time series as a whole, the ATSR and SLSTR datasets are re-evaluated for thermal anomaly activity using the persistent thermal anomaly maps generated using the approach described above. In the case of ATSR, given an overpass of a known persistent thermal anomaly cell in the ATSR 1-arcminute grid, all pixels associated with the grid cell are extracted and, as an initial step, the sensor name, sampling date and time of the overpass are recorded as is the local cloud cover. In the case of SLSTR, the same information is recorded when an overpass of a known persistent thermal anomaly containing cell in either 1-arcminute grid occurs. Both persistent anomaly grids are used for SLSTR to maximise thermal detection opportunity as the reduced sampling opportunities likely lead to many flaring sites being missed, particularly in cloudy regions.

For the ATSR and SLSTR sensors, pixel level cloud cover is computed as:

$$\overline{C}_x = \frac{\sum_n C_n \sim G_n}{\sum_n \sim G_n} \tag{2}$$

where $\overline{C}$ is the local mean cloud cover for a pixel, x, located in a 1-arcminute grid cell, and C is the ATSR or SLSTR standard cloud mask product, $\sim G$ is the 1's complement of the thermal anomaly binary flag (to avoid thermal anomalies, which are often mis-flagged as cloud) and $n \in N$ where N is a 9 × 9 (if ATSR) or 17 × 17 (if SLSTR, due to higher imaging resolution) pixel window centred on x. The local mean cloud cover for the grid cell is then the mean $\overline{C}_x$ over all pixels x contained within. For all x located in the grid cell that contain an active thermal anomaly (i.e. $G_x = 1$) the FRP is calculated using Eq. (3) (see Section 2.5) and the outputs summed to provide a grid cell total, the mean 1.6 μm reflectance (for ATSR) or spectral radiance (for SLSTR) for these pixels is also recorded as is the mean 2.2 μm spectral radiance in the case of SLSTR and the mean 3.7 μm spectral radiance for non-saturated pixels in case of AATSR and ATSR-2 (if all MWIR pixels are saturated a null value is recorded). To adjust the MWIR observations for background contributions local mean MWIR background radiances are calculated over a 9 × 9 window using a similar approach to Eq. (2) but excluding any cloudy pixels in addition to those containing thermal anomalies. If < 60% of the MWIR background pixels are found to be suitable then a null value is recorded for the grid cell mean MWIR background. In the case of ATSR-1 all MWIR background values are set to null values due to the early 3.7 μm channel failure in May 1992. All data described here are produced every time a known thermal anomaly grid cell is overpassed, providing detailed information on sampling, cloud cover statistics and thermal anomaly radiant activity, and various useful sensor radiance values at 1-arcminute resolution globally for all identified persistent thermal anomalies across all four imaging systems.

2.5. FRP calculation

FRPs for each identified thermal anomaly pixel are calculated using the SWIR-radiance method of Fisher and Wooster (2018), which builds on the MWIR-radiance approach previously developed by Wooster et al. (2003) and Wooster et al. (2005) for landscape fires. Estimates of industrial gas flare FRP with a ± 13.6% uncertainty can be calculated using this approach, without knowledge of the emitter temperature (beyond that it is a gas flare and thus has combustion temperatures in the 1600–2200 K range) (Fisher and Wooster, 2018).

$$FRP_{SWIR} = A_s \frac{\sigma}{a} L_{SWIR} \tag{3}$$

where FRP_{SWIR} is the power (W) emitted from the thermal anomaly contained within the pixel, A_s is the area of the pixel (m^2), σ is the Stefan-Boltzmann constant (5.67×10^{-8} W m^{-2} K^{-4}) and $\frac{\sigma}{a}$ is referred to as the FRP coefficient (in sr·μm) that maps from spectral radiance to radiant emittance. Optimised values of a (Table 1) are derived using the

Table 1
Sensor-specific FRP coefficients ($\frac{\sigma}{a}$) for use in Eq. (1).

Sensor	FRP coeff.
ATSR-1	6.88 sr·μm
ATSR-2	6.90 sr·μm
AATSR	6.83 sr·μm
SLSTR	6.92 sr·μm
VIIRS	7.32 sr·μm

sensor specific SWIR band spectral response functions of ATSR-1, ATSR-2, AATSR and SLSTR. The spectral radiance values L_{SWIR} for ATSR are inverted from the spectral reflectance data stored in the Level-1b products assuming the following in-band solar exoatmospheric irradiances ($\mathrm{W\,m^{-2}\,sr^{-1}\,\mu m^{-1}}$): ATSR-1: 250.728; ATSR-2: 249.604 AATSR: 254.752. SLSTR spectral radiance values are provided in the standard Level-1b product. Since the SWIR observations are made within a high transmission atmospheric window (and our FRP data are converted to BCM using a simple linear factor derived from a regression (Section 4.3)) we do not apply adjustments for variable atmospheric state, it previously having been demonstrated that there is a strong linear relationship between FRP derived using top-of-atmosphere and atmospherically corrected SWIR spectral radiances (Elvidge et al., 2015, 2013). ATSR pixel areas for use in Eq. (3) were calculated using the approach defined in Prata et al. (1990) that models ATSR pixels as an ellipse, and is here parameterised using the ATSR scan geometry approximations defined in Denis et al. (2007). In the case of SLSTR the pixel area estimates used were provided by STFC-Rutherford Appleton Laboratory from a detailed instrument model (D. Smith, pers. comm.).

2.6. Persistent thermal anomaly type determination

The persistent thermal anomaly sites identified using the methods outlined in Section 2.4 are mostly associated with flaring and non-flaring industrial activities, along with a far smaller percentage from volcanic activity and misclassified SAA and biomass burning features. In Casadio et al. (2012) those associated with volcanism are removed using data from the Global Volcanism Program (Global Volcanism Program, 2013) on recently active volcanoes. However, no further discrimination based on different types of industrial activity is made. This limitation was overcome in Elvidge et al. (2015) where temperature estimates are produced for every thermal anomaly via a Planck fitting approach applied to multi-spectral VIIRS observations. This temperature information is generally effective for discriminating between thermal anomalies associated with typically cooler non-flaring industrial activities (with retrieved radiometric temperatures in the range of 600–1200 K (Elvidge et al., 2015)) and hotter gas flaring activity (with retrieved radiometric temperatures in the range of 1600–2150 K (Elvidge et al., 2015, 2013; Leifer et al., 2012; Reed, 1986)). Here we introduce a further method, based on a simple two channel ratio method.

2.6.1. Spectral ratio method

In plot (a) of Fig. 1 ratios for central wavelengths of spectral channels found on ATSR-2/AATSR (1.6 μm/3.7 μm) and SLSTR (S5 (1.6 μm)/S7 (2.2 μm)) are shown over a range of temperatures covering biomass burning, non-flaring industrial activities and industrial gas flaring. As emitter temperature increases so does this spectral radiance ratio and, as it increases monotonically, under a grey-body assumption it is possible to define thresholds to discriminate between different temperature features (Fisher and Wooster, 2018). This outcome is a direct result of Wien's Displacement Law, which results in a greater proportion of total emitted radiance occurring at shorter wavelengths as emitter temperature increases.

For the ATSR-2/AATSR sensors, the 1.6 μm and 'above background' 3.7 μm radiances for a given 1-arcminute grid cell are used in the ratio computation. Any data contained in the cell time series from ATSR-1 are excluded from the ratio calculation for the reasons given in Section 2.1, as are thermal anomaly samples from ATSR-2 and AATSR that are either associated with saturated 3.7 μm observations or contain no valid 3.7 μm background values. The median of all valid ratio values contained in a grid cell is then computed, and their distribution shown in Fig. 1b. If the ratio's median value lies between the calculated range for gas flaring (1.62 to 8.35 $\mathrm{W\,m^{-2}\,sr^{-1}\,\mu m^{-1}}$ $(\mathrm{W\,m^{-2}\,sr^{-1}\,\mu m^{-1}})^{-1}$, corresponding to emitter temperatures of 1400 and 2800 K respectively), then the cell is assumed to be associated with industrial gas flaring. These ratios and their associated temperatures were chosen based on an assumed cross-over combustion temperature (1300–1500 K) between flaring and non-flaring activities, with temperatures near 1400 K appearing as the inflection point (Elvidge et al., 2015) and so used here as the lower threshold. It can be seen from the distribution shown in Fig. 1b that the lower threshold value provides clear discrimination between two different classes (i.e. flaring and non-flaring) of thermal anomaly activity, whilst the upper threshold is of minimal significance since few persistent thermal anomalies other than gas flares combust at temperatures above 1400 K. However, a few thermal anomalies associated with the SAA exhibit very high ratio values, and so an upper limit of 2800 K was chosen to exclude such features from the flaring dataset (ensuring their assignment to the non-flaring class).

In the case of SLSTR, the ratio process is further simplified as only SWIR channels are used, so there is no background contribution to remove and they do not saturate in the presence of even the most highly radiant gas flares. Appropriate ratio values for the SLSTR channels are 0.84 $\mathrm{W\,m^{-2}\,sr^{-1}\,\mu m^{-1}}$ $(\mathrm{W\,m^{-2}\,sr^{-1}\,\mu m^{-1}})^{-1}$ for the lower threshold and 1.93 $\mathrm{W\,m^{-2}\,sr^{-1}\,\mu m^{-1}}(\mathrm{W\,m^{-2}\,sr^{-1}\,\mu m^{-1}})^{-1}$ for the upper threshold (equivalent to emitter temperatures of 1400 K and 2800 K respectively). As with the ATSR sensors, the median spectral radiance ratio values for a given grid cell are computed. The distribution of median ratios for all persistent thermal anomalies is shown in Fig. 1c, where - as with ATSR - a clear discrimination is made between assumed flaring and non-flaring persistent thermal anomalies and excellent spatial agreement with the ATSR classification is seen in the spatial distribution maps shown in Fig. 2a and b.

2.6.2. Unclassified grid cell type assignment

Type classification of persistent thermal anomalies into flaring or non-flaring classes using the methods detailed above was still not fully achieved across all thermal anomaly 1-arcminute grid cells. In the case of ATSR-1, as concurrent operation of the SWIR and MWIR was not possible, the spectral ratio method is not applicable, and the grid cell classification is dependent on the presence of AATSR and ATSR-2 observations. If no such data are available from the other sensors, then classification of ATSR-1 thermal anomaly containing grid cells cannot be performed. Non-assignment also occurs in grid cells containing AATSR and ATSR-2 data under two specific conditions: either when all thermal anomaly MWIR radiances associated with the grid cell are saturated; or when no MWIR background radiance estimates are available to compute the excess MWIR radiance. The first of these conditions can occur in the presence of either extreme gas flaring activity, or at sites of volcanic activity. The second occurs in grid cells with limited thermal anomaly activity and persistent cloud cover. To provide classifications across all ATSR sensors for the unassigned grid cells, a simple majority voting approach is employed where all assigned grid cells from the entire ATSR-2 and AATSR time series within 1° are considered and the unassigned cell is given the majority class.

2.7. Flare activity screening

The spectral ratio histograms in Fig. 1b and c show that there is

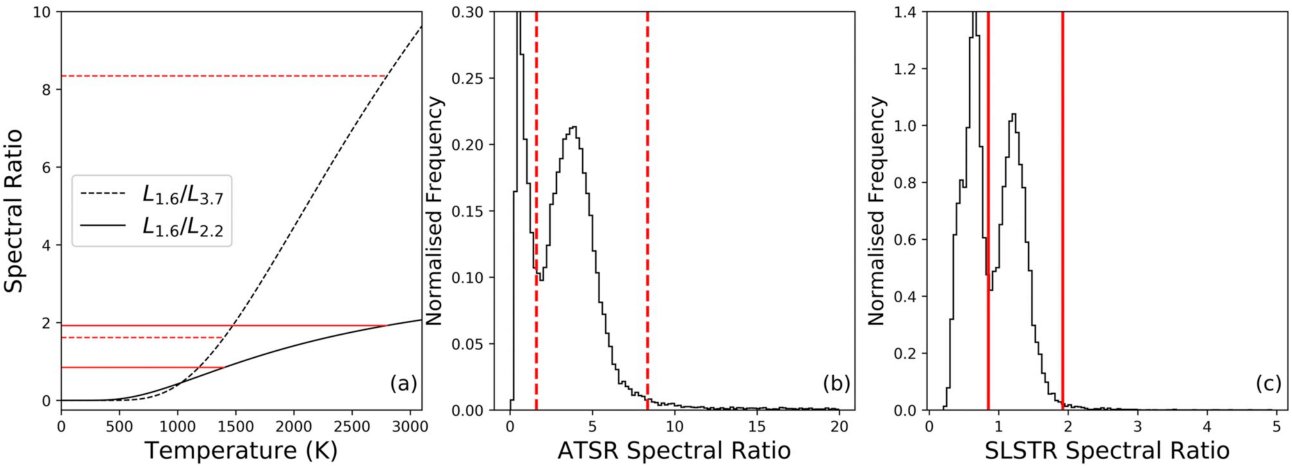

Fig. 1. Spectral radiance ratios for thermal emission from objects at different temperatures, and which encompass biomass burning, gas flaring and non-flaring industrial sites. (a) 1.6 μm to 3.7 μm spectral radiance ratio, along with that for 1.6 μm to 2.2 μm. The ratios are monotonically increasing with increasing emitter temperature above a minimum temperature limit and can be used to discriminate between thermal anomalies associated with different surface features. (b) Normalised histogram of the median 1.6 μm to 3.7 μm spectral radiance ratios found with AATSR and ATSR-2 data for all thermal anomaly containing 1-arcminute grid cells. Red vertical dashed lines show the threshold values associated with 1400 K and 2800 K emitters, a range encompassing gas flaring temperatures (Elvidge et al., 2015, 2013). (c) Normalised histogram of the median 1.6 μm to 2.2 μm spectral radiance ratios found with SLSTR for all thermal anomaly containing grid cells, with a similar ability to clearly delineate gas flaring temperatures from lower temperature thermal anomalies (vegetation fires and non-flaring industrial targets) with red vertical solid lines showing the threshold values associated with 1400 K and 2800 K . (For interpretation of the references to colour in this figure legend, the reader is referred to the web version of this article.)

significant overlap between assumed flaring and non-flaring classes, and therefore incorrect class assignments are very likely to be present in the resulting classification. The majority of these misclassifications will not have significant impact on the resulting statistics, as they are associated with grid cells having very limited sampling (see Supplementary materials Fig. S3). As such, they do not contribute significantly in terms of FRP to global or country level statistics of flaring output. One important exception however, are those grid cells associated with volcanic activity, as some such sites can be highly persistent and radiant (e.g. Mount Nyiragongo, DRC (Burgi et al., 2014)) and so contribute significantly to any FRP statistics computed. To discriminate these sites the Global Volcanism Program data (Global Volcanism Program, 2013) on recently active volcanoes was used, assigning any thermal anomaly grid cell within 10 arc-minutes of an active volcano to the non-flare classification.

Further screening is applied to the remaining ATSR flaring grid cells through exclusion of any sites with time-series FRP mean or standard deviation values exceeding those from the AATSR time series of a flare containing grid cell near the settlement of Punta de Mata, Venezuela [Lat.: 9.69°N; Lon.: 63.62°W], selected as it has the largest observed mean FRP at 70.71 (± 93.16) MW for a visually confirmed flaring site in the dataset. The need for this calibration of flaring activity to that observed by AATSR is shown in Fig. 3, where more extreme mean and standard deviation values are seen across the ATSR-1 and ATSR-2 sensor time series. These outlying grid cells are assumed related to sensor introduced artefacts rather than true radiative emission from gas flaring. Particularly high levels of FRP outliers were found across the northern hemisphere by ATSR-1 during 1994 and 1995, and whilst the cause of these raised FRP signals is currently undetermined the calibration approach employed here removes the more extreme anomalous values from further consideration in the FRP analysis (see Fig. 3). No such screening was applied to SLSTR dataset as the observations are more consistent with the AATSR observed FRP mean and standard deviation values for the Punta de Mata flaring site.

2.8. Gridded dataset summary

Following application of the spectral ratio test to the AATSR and ATSR-2 persistent thermal anomalies, out of a set of unique grid cell counts for the sensor time series of 33,531 and 32,553 respectively, a total of 21,582 and 19,754 1-arcminute grid cells are assigned as flare containing, 10,279 and 9948 cells are assigned to non-flaring activities, and the remaining 1670 and 2851 grid cells are without classification (due to invalid MWIR backgrounds, or saturated MWIR samples). Following application of the majority reassignment approach described in Section 2.6.2, these change to 22,553 and 21,186 grid cells for flaring and 10,978 and 11,367 grid cells for non-flaring activities for AATSR and ATSR-2 respectively. In the case of ATSR-1 a total of 2091 1-arcminute grid cells across the time series do not have any associated AATSR and ATSR-2 data and are thus assigned using the majority assignment approach which delivers a total of 14,426 flaring cells and 6934 non-flaring cells. For SLSTR, a total of 22,452 persistent thermal anomalies are identified, of which 10,431 flaring cells and 12,021 non-flaring cells are found across the time series after application of the spectral ratio test of Section 2.6.1. The volcano proximity test results in the exclusion of an additional 33 grid cells in ATSR-1, 64 grid cells in ATSR-2, 66 grid cells in AATSR, and 3 grid cells in SLSTR not excluded by the spectral ratio test. For the ATSR sensors, the use of the AATSR observation of the Punta de Mata flaring site as an upper limit on FRP results in the exclusion of 2296 grid cells from ATSR-1, 3218 grid cells from ATSR-2, and 1192 from ATS. Whilst these counts may appear to be high, they are in fact associated with only 0.8%, 0.6% and 0.07% of the totalled gas flaring FRP for the ATSR-1, ATSR-2 and AATSR datasets respectively. The final flare containing 1-arcminute grid cell counts for all sensors across their respective time series and those flares that are common to all ATSR sensors are shown in Table 2.

Annual total sampling and mean cloud cover statistics are shown for the identified flaring grid cells on an annual and sensor basis in Table 3. Increased sampling (for completely sampled years) is observed progressing through the sensors, with ATSR-1 typically having ~1.9 million samples across all 1-arcminute grid cells per annum, for ATSR-2 the typical number is ~2.1 million, and for AATSR ~2.4 million. Differences are related primarily to variations in the number of flares operating in any given year. Additionally, as mentioned in Section 2.2, for certain years ATSR does not have complete sampling: For ATSR-1 reduced sampling is available in the first (1991) and last (1996) years of operation (Table 3); for ATSR-2 the operational issues in 1996 and 2001 and the use of AATSR data from May 2002 are reflected in the sample

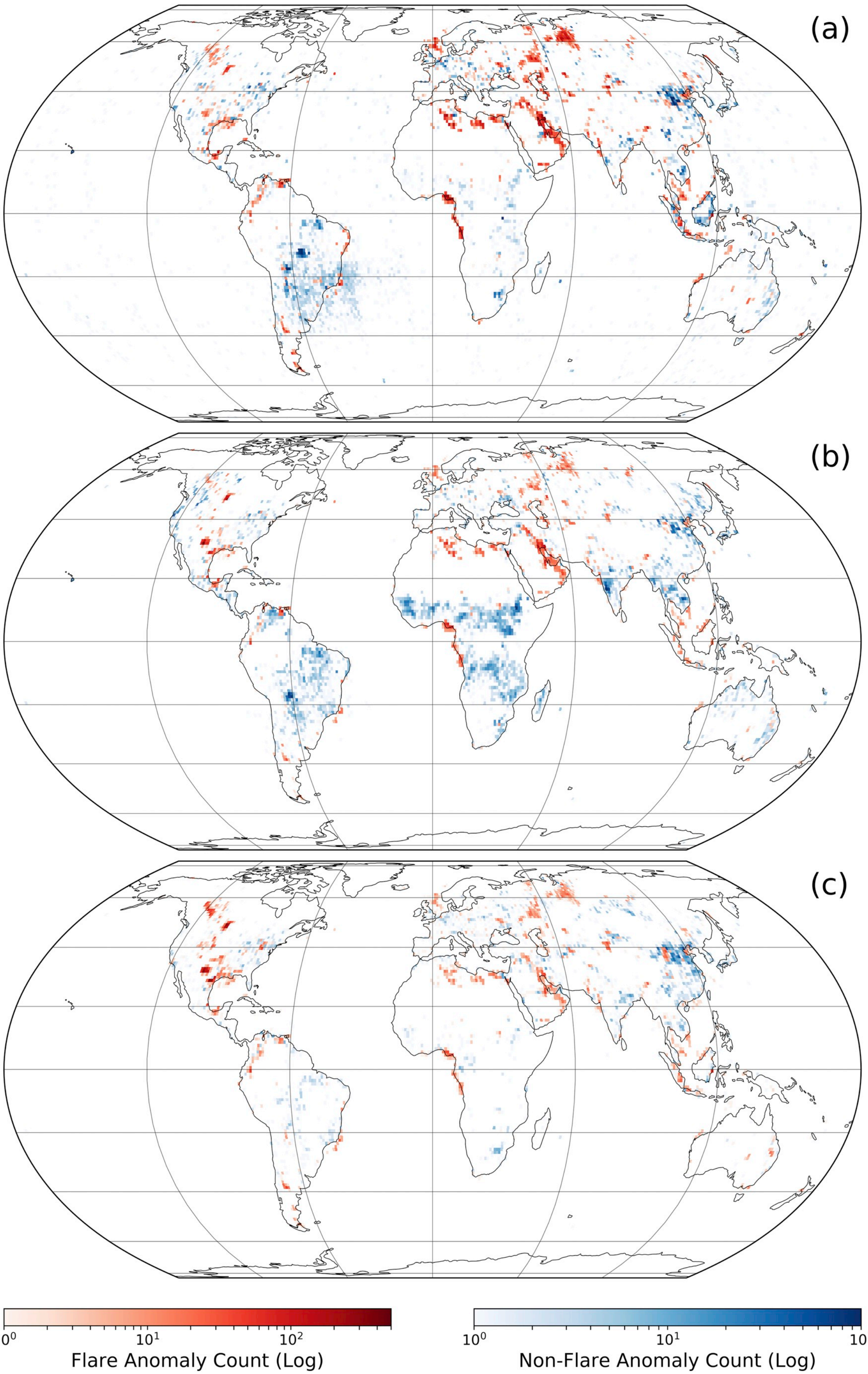

(caption on next page)

Fig. 2. The total number of flaring (red shades) and non-flaring (blue shades) unique 1-arcminute grid cells, aggregated into 1° bins (and retaining the dominant class), are shown for the sensors used in this study. Notice that log colour scales have been applied. The classification is achieved using the spectral radiance ratio method described in Section 2.6.1. Map (a) shows the ATSR-1, ATSR-2 and AATSR unique thermal anomaly detections for the time period August 1991 through April 2012. Map (b) shows the unique thermal detections for SLSTR data for the time period May 2017 to May 2018. Map (c) shows the unique thermal detections taken from the output of the enhanced VIIRS NightFire algorithm (Liu et al., 2018) discussed in Section 3.1 and which covers the time period September 2012 to September 2016. (For interpretation of the references to colour in this figure legend, the reader is referred to the web version of this article.)

counts; and for AATSR reduced sampling affects the final 2012 year of operation (Envisat failed in April of that year).

Given the global distribution of persistent thermal anomalies (see maps in Fig. 2), averaging the local cloud cover statistics over all grid cell samples should result in a value of ∼60%, and this is the case for the ATSR-2 and AATSR sensors. For ATSR-1 the value is nearer ∼40% and is likely a result of the failure of 3.7 µm channel and the resulting deficiencies in cloud masking stemming from use of only 11 µm and 12 µm observations at night. This issue and its resolution are discussed further in Section 4.2. For SLSTR the reported cloud cover mean is also too low and is also caused by deficiencies in the current SLSTR Level-1b cloud masking procedures at the time of processing. The issue is resolved using the same method as applied to ATSR-1 discussed in Section 4.2.

3. Dataset validation

3.1. Assessment of flare detection

Section 2.3 already identified existing datasets mapping persistent thermal anomalies, though most do not separate these into thermal anomaly classes. Segregation is attempted in the VIIRS NightFire product by exploiting the typically higher combustion temperatures (> 1600 K) of gas flares, thus classifying persistent anomalies on the basis of their retrieved effective emitter temperatures (Elvidge et al., 2015). Further sophistication was introduced by Liu et al. (2018), where persistent NightFire thermal anomalies are assigned to one of four different classes (cement production; smelting processes; coal powered energy generation and chemical processing; and oil and gas related activities) based on their temperature distribution compared to a set of supervised learning derived Gaussian mixture models. Excellent classification accuracy was reported (Liu et al., 2018), and over three different validations, involving the supervised learning database, a site-specific validation performed for two regions of interest in China, and an extended global validation, respective user accuracies of ∼100% (across 53,547 samples), ∼82% (across 57 samples) and ∼88% (across 585 samples) were found. Outputs from this approach were selected to provide the validation dataset for assessing the performance of the persistent thermal anomaly classification approach developed herein for ATSR and SLSTR (detailed in Section 2).

Table 2
Total unique flare counts across the various sensor time series, with each 1-arcminute grid cell containing flaring representing a single "flare count".

Sensor	Flare count
ATSR common	26,083
ATSR-1	12,097
ATSR-2	17,904
AATSR	21,295
SLSTR	10,428

The VIIRS NightFire time series reported in Liu et al. (2018) extends from 1st September 2012 to 1st September 2016, with no temporal intersections between this and the ATSR (August 1991 to April 2012) or SLSTR (May 2017 to May 2018) dataset developed herein. However, since gas flares typically operate (sporadically) for many years, significant overlap of flaring locations across the various time series is found. Mean flare operation duration across all 26,083 locations sampled by ATSR is 4018 ($\sigma = \pm 2360$) days for example, equating to more than a decade of operation typically. To assess the similarity between the NightFire classification and the ATSR/SLSTR classifications, the former was resampled from its 15-arcsecond resolution grid (∼500 m) to a 1-arcminute grid, with the mode used as the aggregation statistic (Fig. 2c), where the four original classes are re-binned into either flaring (i.e. class 4) or non-flaring (i.e. classes 1–3) persistent thermal anomalies. Comparing qualitatively the maps of Fig. 2 it is apparent that there are distinct similarities in the spatial distributions of flaring activity across VIIRS, ATSR and SLSTR. The most striking difference is the significant spatial increase in flaring extent and density in the USA and Canada in the VIIRS NightFire product compared to that observed in the datasets generated here. An initial statistical comparison is shown in Table 4, where for each sensor's gridded dataset the grid cells associated with flaring are compared against those from the

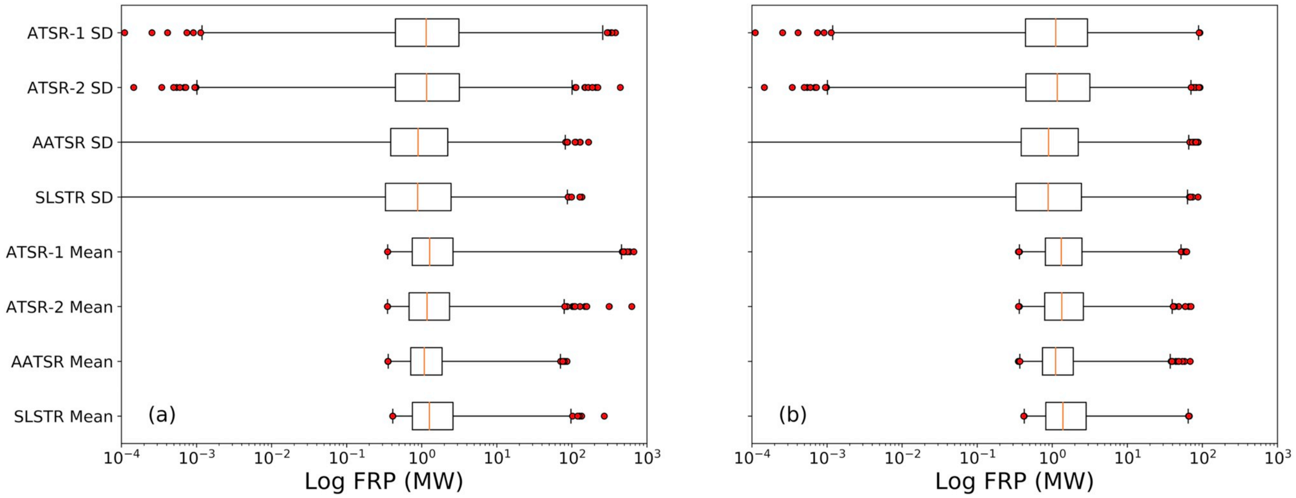

Fig. 3. Flare FRP 1-arcminute grid cell mean and standard deviation distributions for each sensor before (a) and after (b) screening based on the activity of the most highly radiant flaring grid cell in the AATSR time series located near Punta de Mata, Venezuela [Lat.: 9.69°N; Lon.: 63.62°W].

Table 3
Annual sampling totals (S, millions) and global annual mean cloud cover (C, fractional) for all 1-arcminute flaring grid cells through the data time-series. For cloud cover reported for ATSR-1 and SLSTR, the value in parenthesis is the mean global cloud cover prior to the correction detailed in Section 4.2.

Year		'91	'92	'93	'94	'95	'96	'97	'98	'99	'00	'01	–
ATSR-1	S	0.71	1.75	1.90	1.91	1.84	0.88	–	–	–	–	–	–
	C	0.60 (0.56)	0.60 (0.47)	0.60 (0.37)	0.60 (0.34)	0.60 (0.38)	0.60 (0.41)	–	–	–	–	–	–
ATSR-2	S	–	–	–	–	–	1.10	2.18	2.13	2.05	2.10	1.82	–
	C	–	–	–	–	–	0.60	0.60	0.60	0.61	0.62	0.62	–

Year		'02	'03	'04	'05	'06	'07	'08	'09	'10	'11	'12	'18
ATSR-2	S	0.45	–	–	–	–	–	–	–	–	–	–	–
	C	0.66	–	–	–	–	–	–	–	–	–	–	–
AATSR	S	1.32	2.35	2.42	2.46	2.37	2.43	2.51	2.49	2.44	2.47	0.75	–
	C	0.59	0.60	0.60	0.59	0.60	0.60	0.61	0.60	0.60	0.60	0.63	–
SLSTR	S	–	–	–	–	–	–	–	–	–	–	–	0.9
	C	–	–	–	–	–	–	–	–	–	–	–	0.57 (0.41)

Table 4
Comparison between flare detections made by ATSR, SLSTR and VIIRS. Reported percentages show proportion of the total number of observed 1-arcminute grid cells in the source data having gas flaring activity in the matched data. Three columns at left are for all grid-cells, and at right for those excluding the United States, Canada or China (the reasons for which are discussed in section 3.2).

		Matched					
		All cells			Excl. USA, Canada, China		
		ATSR	SLSTR	VIIRS	ATSR	SLSTR	VIIRS
Source	ATSR	–	46%	34%	–	49%	34%
	SLSTR	64%	–	50%	77%	–	49%
	VIIRS	36%	35%	–	60%	49%	–

two alternative sensors. A flare containing 1-arcminute grid cell is considered to be matched if any collocated or touching (edges and corners) alternative sensor grid cell also contains gas flaring; the reported statistic is the ratio of matched flare grid cells to their total number. These global statistics show that the greatest agreement is for SLSTR flaring grid cells matched by an adjacent ATSR flare containing cell at ~64% of locations. In comparison, ~46% of ATSR detections are matched by adjacent SLSTR cells. These outcomes are reasonable, as the spatial distribution of flaring activity towards the end of the ATSR observational period is likely more similar to that of SLSTR than the spatial distribution of the SLSTR flaring activity is to that of ATSR in the earlier stages of its operation. Of the ATSR flaring sites ~34% are seen in the enhanced VIIRS NightFire product, and for SLSTR ~50%, an increase to be expected since the temporal ranges covered by VIIRS and SLSTR are more similar than VIIRS and ATSR. Assessing the VIIRS product, ~36% of flare containing grid cells are seen by ATSR and ~35% by SLSTR, and from Fig. 2 it can be seen that a large proportion of these missed matches originate from the United States and Canada (this is evaluated further in section 3.2).

To better assess the impact of this apparent variation in flaring activity between sensors, Fig. 4 shows the same analysis performed at the global scale in Table 4, but now applied at a national level for the top 20 flaring countries (based on a ranking determined from the enhanced NightFire (Liu et al., 2018) data gas flaring grid cell counts, but with the number assessed chosen arbitrarily). The reported national level statistics clearly reflect the global outcomes in most instances. For ATSR the percentages of matched grid cells range from ~21% (Kazakhstan) to ~50% (Indonesia) when assessing against VIIRS, and from ~23% (China) to ~75% (Iran) when assessing against SLSTR. The percentage of matched cells for SLSTR ranges from ~33% (Iraq) to ~77% (Indonesia) with VIIRS and, excluding the United States (at ~18%), from ~43% (Canada) to ~95% (Libya) with ATSR. Lastly, for VIIRS the approximate matching percentage ranges for ATSR and SLSTR are similar, with all but three countries between ~30% (Argentina – SLSTR) and ~90% (Libya – ATSR). The three exceptions are the USA, Canada and China with matched percentages of ~9%, ~12%, and ~27% and ~24%, ~9%, and ~17% for ATSR and SLSTR respectively, corresponding with the spatial distributions of Fig. 2. Further analysis on the causes of these differences is performed in Section 3.2, with a case study on data from the United States and Canada. Updated global matching statistics with these three outlying countries removed are shown in Table 4, and particular improvements are found when evaluating using VIIRS, with a ~24% increase in the matched proportion to ~60% with ATSR and a ~14% increase with SLSTR to ~49%. A substantial improvement is also seen for SLSTR when considering adjacent ATSR cells, increasing by ~13 percentage points to a 77% agreement between the sensors. The level of agreement shown, particularly in the case of SLSTR and matching ATSR grid cells, is encouraging, with the difference in the case of SLSTR assumed to be due to flare commissioning/decommissioning activities between the periods of operation of the relevant sensors. The larger differences in the VIIRS assessment are assumed, in part, to be enhancements caused by differences in the imaging geometry and detection algorithm used (see Section 3.2 for further discussion). A more modest improvement is found for ATSR cells matched by an adjacent SLSTR cell, increasing by ~3 percentage points to ~49%, an expected result as the matched flaring activity in the excluded and retained countries is consistent (see Fig. 4). Similarly, when assessing the ATSR and SLSTR grids with VIIRS, no change is found for the former at 34%, and a small deterioration in matching performance is found for the latter, decreasing by ~1 percentage point to ~49%. Which again is expected, as the flaring activity in the three excluded countries is consistent with those that are retained (again see Fig. 4).

3.2. *Flare detection case study: VIIRS vs. SLSTR over the United States and Canada*

Section 3.1 demonstrated that VIIRS and the enhanced NightFire algorithm employed detects far more flaring activity across Canada, the United States and China than do ATSR or SLSTR. This is partly due to actual increases in active flaring sites, as indicated during the transition from ATSR to SLSTR over the United States (with no such effect seen for China or Canada, see Fig. 4b). However, if it were caused by increased flare counts alone then, given their more similar period of operation, SLSTR would be expected to detect a similar number of flaring sites as VIIRS, yet it misses ~76% of them in the case of the United States for example. To ascertain the cause, VIIRS NightFire data within continental United States and Canada for December 2017 were retrieved from the NOAA National Centre for Environmental Information

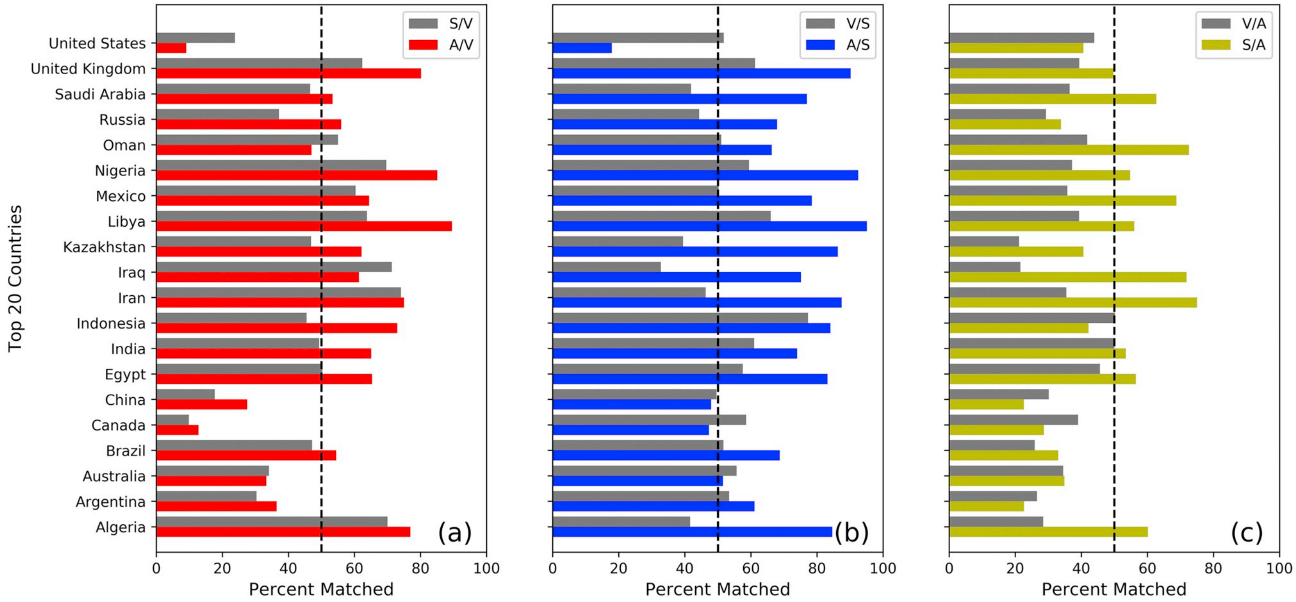

Fig. 4. Matched gas flare detections by country. Histograms denote the percentage of 1-arcminute grid cells detected by (a) VIIRS, (b) SLSTR, and (c) ATSR that have a matched detection from an alternate sensor within 1-arcminute grid cell. In each legend, the V, S and A denotes VIIRS, SLSTR and ATSR respectively.

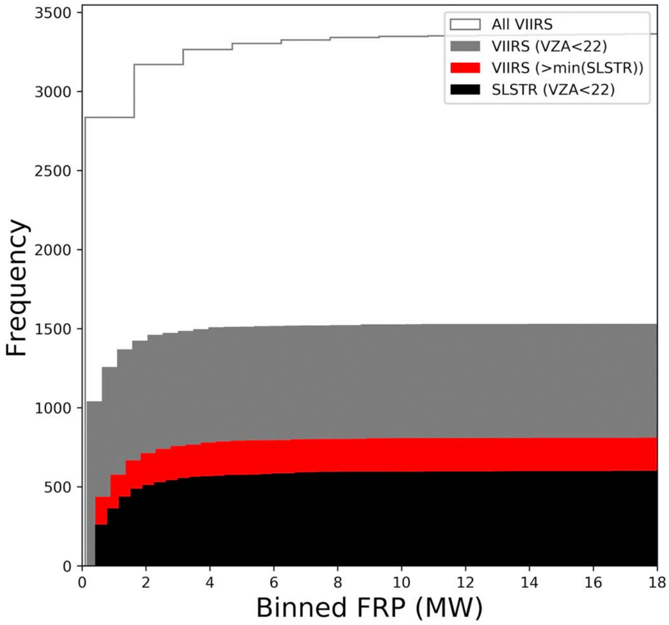

Fig. 5. Cumulative counts of FRP over the United States and Canada for December 2017 for the VIIRS NightFire product and the SLSTR gas flaring dataset herein generated. Various view zenith angle (VZA) thresholds have been applied to the VIIRS NightFire data, and these are referred to in the plot legend and in Section 3.2.

(https://ngdc.noaa.gov/eog/viirs/download_viirs_fire.html). Assuming limited landscape fire activity during this winter period (Zhang et al., 2014), all VIIRS NightFire hotspots with Planck fit temperatures exceeding 1400 K were reasonably assumed (Elvidge et al., 2015, Fig. 1) to be associated with industrial gas flaring locations. The basic processing involved resampling the subset data to a 1-arcminute grid with all unique grid cells with recorded flare activity flagged. Two different thresholds were then iteratively applied to the spatially subset NightFire data: the first restricted the VIIRS view zenith angle (VZA) of the NightFire observations to a maximum of 22°, the same restriction applied to the SLSTR data and reflecting the maximum VZA of the ATSR nadir view; the second rejected all NightFire detections with a mean FRP less than the smallest mean value for all active flare sites observed by SLSTR in study region and period. The objective was to create an SLSTR like product from the VIIRS NightFire data, and the cumulative histograms shown in Fig. 5 show that the process has resulted in SLSTR and VIIRS flare counts for the assessment region and period that are far more similar (within ~30% of one other), a result consistent with the country level analysis shown in Fig. 4. This outcome indicates that flares recently commissioned in the United States and Canada, assumed to be associated with shale gas developments, are less radiant and more dynamic and/or less persistent than those associated with more traditional extractive processes such as for oil, confirming findings made by (Liu et al., 2018). The remaining differences in flaring activity recorded between the sensors, seen here and in Section 3.1, are assumed to be due to inter-timeseries commissioning/decommissioning of flares, differing thermal anomaly sensitivity of the two sensors (e.g. due to signal to noise ratio, VIIRS' smaller pixel area that is better maintained across the swath), and, in the case of VIIRS, differences in the detection and screening methodologies employed in the identification of flaring sites, the most significant of which is the exclusion of sites associated with flare detection in only the SWIR channel in the enhanced VIIRS dataset used herein (Liu et al., 2018).

3.3. Assessment of flare characterisation

In Fisher and Wooster (2018) an extensive validation of the SWIR-radiance approach for estimating gas flare FRP was conducted. A more limited evaluation is undertaken here, comparing AATSR and SLSTR derived FRP against VIIRS, with the objective of assessing the degree of consistency between the two systems' characterisations. Excellent inter-system radiometric calibration has been reported for the ATSR sensors (Smith et al., 2012; Smith and Cox, 2013), though high biases have been reported for the SWIR channels of SLSTR over various surface types (Smith, 2018), and here we assess the appropriateness of the suggested 12% upward adjustment factor for the S5 band nadir view spectral radiances. For an ROI located in Southern Iraq (Lat. range: 20°N – 36°N; Lon. range: 42°E – 60°E), containing a significant proportion of the most radiant flares globally (see Fig. 11), all intersecting night-time VIIRS M10 SDR granules were retrieved from the NASA Level-1 and Atmosphere Archive and Distribution System (LAADS; ww.ladsweb.modaps.eosdis.nasa.gov) for March 2012 and March 2017. The

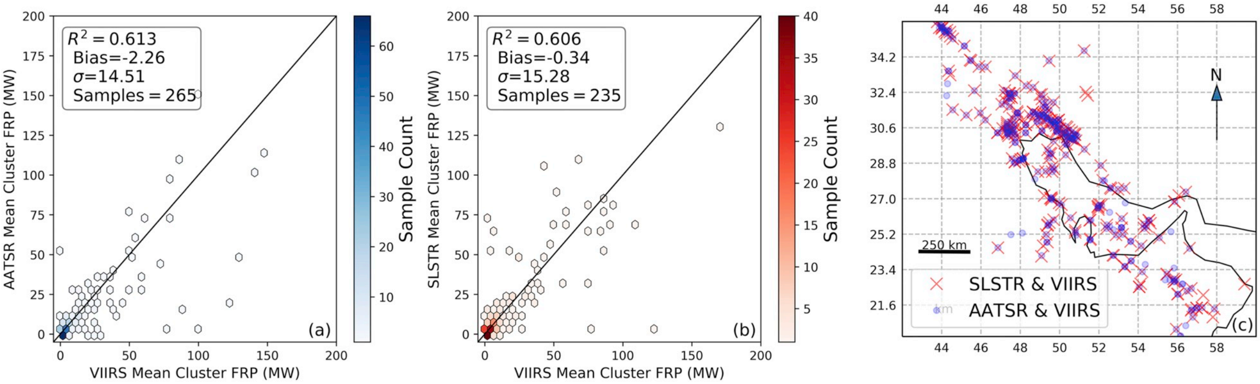

Fig. 6. Plot (a) shows the joint histogram FRP estimates (MW) from AATSR and VIIRS over the study ROI shown in plot (c) and located in Southern Iraq (Latitude range: 20°N – 36°N; Longitude range: 42°E – 60°E) for observations for March 2012. Plot (b) shows for the same region the joint histogram for SLSTR and VIIRS for observations for March 2017. Plot (c) shows the matched detections of gas flaring activity for ATSR and SLSTR against VIIRS for the 0.1-degree grid used in the assessment in Section 3.3.

first processing step involved masking each M10 granule to only those pixels with satellite VZAs of < 22° (to maintain a consistent range with that of the ATSR sensors), and this was followed by the application of a simple statistical thresholding approach, similar to that used in the original NightFire algorithm (Elvidge et al., 2015), where any pixel more than four sigma from the image mean is considered a thermal anomaly. All identified thermal anomalies have their FRP calculated using the SWIR radiance method, applying Eq. (1) with the VIIRS appropriate FRP coefficient defined in Table 1 and VIIRS pixel areas calculated with the approach described in Elvidge et al. (2013). The resultant FRP values were summed into 0.1° daily grids, with monthly means for the 2012 and 2017 observations then computed from the daily aggregated data. It should be noted that this averaging approach does result in some biasing of the FRP estimates (see Section 4.2), but this is of no consequence for our inter-sensor comparison as the same averaging method was applied to generate the 0.1° AATSR and SLSTR monthly mean grids to which the VIIRS data were compared.

All 0.1° grid cells with collocated observations for VIIRS and AATSR for March 2012 are shown in Fig. 6c, and as shown in Fig. 6a across 265 collocated cells a mean bias of −2.3 (± 14.5) MW and a median bias of −0.02 MW are found, indicating small biases between the FRP observations made by the different sensors and techniques. Similarly, the collocated observations for VIIRS and SLSTR for March 2017 shown in Fig. 6b and c demonstrate a small mean FRP bias of −0.34 (± 15.28) MW and a median bias of 0.02 MW across 235 collocated grid cells. The adjustment factor applied to the SLSTR S5 spectral radiances thus appears entirely appropriate for gas flaring.

4. Multiscale gas flaring activity analyses

Here we examine the spatial and temporal variability in gas flaring based on our ATSR and SLSTR records. Consistent with prior studies (Casadio et al., 2012; Elvidge et al., 2015, 2009), we report flaring activity annually at global and national spatial scales (the latter defined via a combination of exclusive economic zone maritime boundaries and national borders from Marine Regions (2018)). Estimates of flared gas volume (in BCM) are generated by calibrating the national level FRP measures produced herein to the national level BCM estimates produced from the DMSP satellite in Elvidge et al. (2009).

4.1. Number of active flare sites

The global flare counts reported in Fig. 7a were generated by counting all unique 1-arcminute grid cells containing flaring activity in any given year. It should be reiterated that certain years in the ATSR data – 1991, 1992, 2001, 2002 and 2012, see Supplementary material Fig. S2 – are incompletely sampled, resulting in biased counts, and also that the statistics generated are not representative of the total number of active flares globally, but rather the total number of 1-arcminute grid cells containing flare activity. The true number of gas flares will be higher but is not determinable at the 1 km resolution of ATSR, nor the 500 m resolution of SLSTR, since they are subpixel. The percentage contribution to the annual global flare counts for the top 30 nations (chosen as typically around 95% of the global flare FRP output is produced by these 30 nations) is shown in Fig. 7b, with the ranking determined by summing the proportions across the time series. The annual change in the proportion of the global activity for each country for completely sampled years is shown in Fig. 7c, highlighting substantial changes in total flaring counts in some nations. Russia is the predominant gas flaring nation, making up > 20% of the total global flaring sites identified each year. Between 2011 and the 12-month period assessed for SLSTR between May 2017 and May 2018 (labelled as 2018), Russia also shows the largest drop in flaring activity, with a ~5% decrease in its global share. Most other nations also show declines over the same period, albeit of lower magnitudes, and this is reflected in a reduction in the total number of 1-arcminute 'flaring' grid cells from ~13,400 in 2011 to ~10,400 in 2018. The United States developed the greatest number of flaring sites in the intervening years between 2011 and the 12-month period assessed for SLSTR, recording a ~14% increase to ultimately possess ~18% of global gas flaring locations (~1900 sites). The US then supersedes Russia as the nation with the most gas flaring sites and, given the analysis on flaring characteristics in the United States and Canada presented in Section 3.2, it should be noted that the count reported here is likely substantially underestimated (the effects of this on radiant outputs are discussed in the next section). In Liu et al. (2018) the total flaring count reported for the United States using the enhanced NightFire dataset is 3441 sites (~31% of all oil/gas related persistent thermal anomalies therein), and this too is likely a low biased estimate considering that a proportion of the flaring activity has likely been excluded due to the rejection of thermal anomalies registered only in the SWIR channel (Liu et al., 2018). What is consistent across recent studies and the work herein is that, due to rapidly expanding shale gas developments, the United States now shows the largest number of gas flaring sites, contrasting with an otherwise significant global reduction in flaring locations globally.

4.2. Estimated total radiant outputs

Given the global distribution and intermittent operation of gas flares, and also the incomplete sampling achievable from satellite EO, effective normalisation is required to compare radiative outputs across different sites (Elvidge et al., 2015; Faruolo et al., 2018). This is

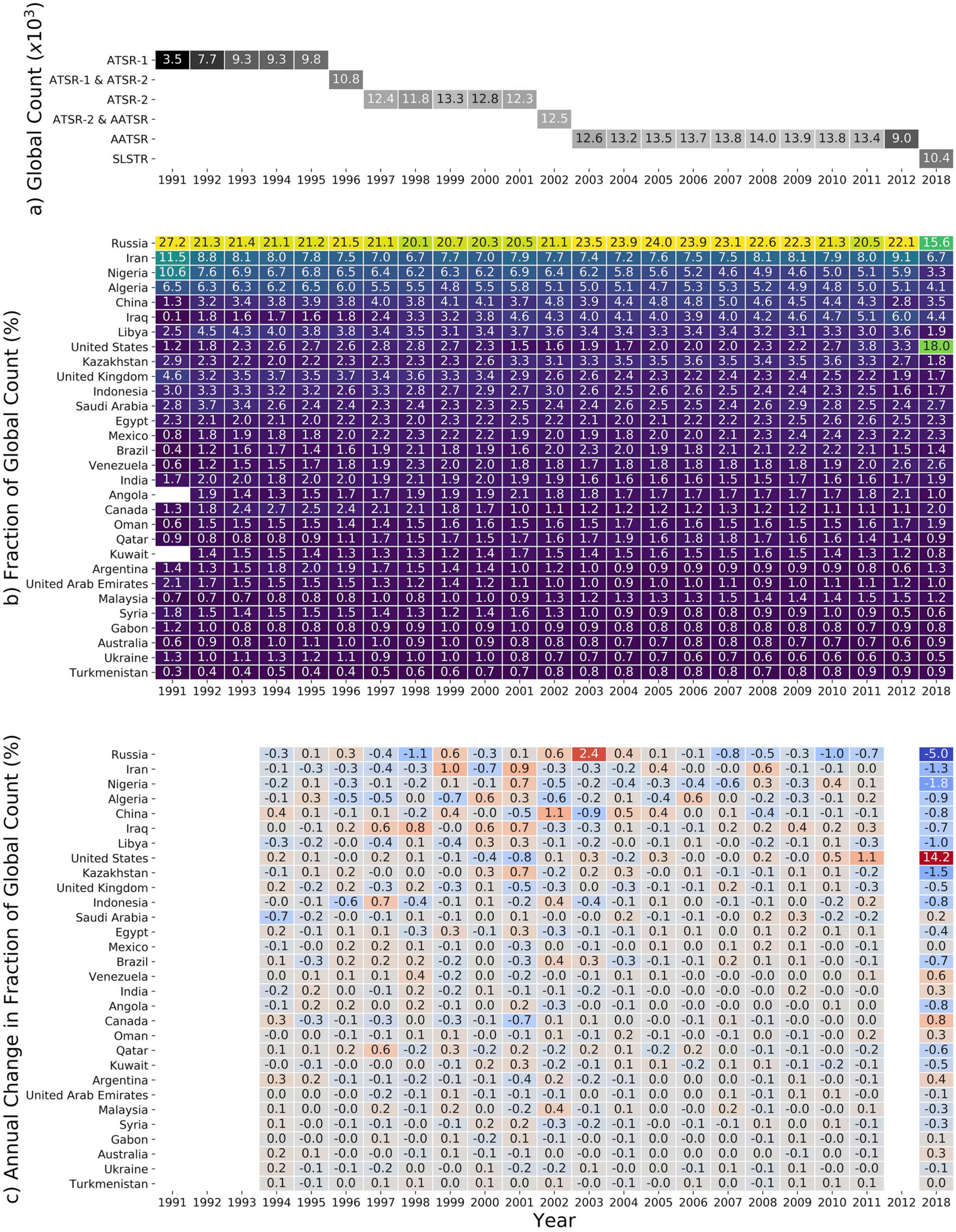

	1991	1992	1993	1994	1995	1996	1997	1998	1999	2000	2001	2002	2003	2004	2005	2006	2007	2008	2009	2010	2011	2012	2018
ATSR-1	3.5	7.7	9.3	9.3	9.8																		
ATSR-1 & ATSR-2						10.8																	
ATSR-2							12.4	11.8	13.3	12.8	12.3												
ATSR-2 & AATSR												12.5											
AATSR													12.6	13.2	13.5	13.7	13.8	14.0	13.9	13.8	13.4	9.0	
SLSTR																							10.4

	1991	1992	1993	1994	1995	1996	1997	1998	1999	2000	2001	2002	2003	2004	2005	2006	2007	2008	2009	2010	2011	2012	2018
Russia	27.2	21.3	21.4	21.1	21.2	21.5	21.1	20.1	20.7	20.3	20.5	21.1	23.5	23.9	24.0	23.9	23.1	22.6	22.3	21.3	20.5	22.1	15.6
Iran	11.5	8.8	8.1	8.0	7.8	7.5	7.0	6.7	7.7	7.0	7.9	7.7	7.4	7.2	7.6	7.5	7.5	8.1	8.1	7.9	8.0	9.1	6.7
Nigeria	10.6	7.6	6.9	6.7	6.8	6.5	6.4	6.2	6.3	6.2	6.9	6.4	6.2	5.8	5.6	5.2	4.6	4.9	4.6	5.0	5.1	5.9	3.3
Algeria	6.5	6.3	6.3	6.2	6.5	6.0	5.5	5.5	4.8	5.5	5.8	5.1	5.0	5.1	4.7	5.3	5.3	5.2	4.9	4.8	5.0	5.1	4.1
China	1.3	3.2	3.4	3.8	3.9	3.8	4.0	3.8	4.1	4.1	3.7	4.8	3.9	4.4	4.8	4.8	5.0	4.6	4.5	4.4	4.3	2.8	3.5
Iraq	0.1	1.8	1.6	1.7	1.6	1.8	2.4	3.3	3.2	3.8	4.6	4.3	4.0	4.1	4.0	3.9	4.0	4.2	4.6	4.7	5.1	6.0	4.4
Libya	2.5	4.5	4.3	4.0	3.8	3.8	3.4	3.5	3.1	3.4	3.7	3.6	3.4	3.4	3.3	3.4	3.4	3.2	3.1	3.3	3.0	3.6	1.9
United States	1.2	1.8	2.3	2.6	2.7	2.6	2.8	2.8	2.7	2.3	1.5	1.6	1.9	1.7	2.0	2.0	2.0	2.3	2.2	2.7	3.8	3.3	18.0
Kazakhstan	2.9	2.3	2.2	2.0	2.2	2.3	2.3	2.3	2.3	2.6	3.3	3.1	3.3	3.5	3.5	3.6	3.5	3.4	3.5	3.6	3.3	2.7	1.8
United Kingdom	4.6	3.2	3.5	3.7	3.5	3.7	3.4	3.6	3.3	3.4	2.9	2.6	2.6	2.4	2.3	2.2	2.4	2.3	2.4	2.5	2.2	1.9	1.7
Indonesia	3.0	3.3	3.3	3.2	3.2	2.6	3.3	2.8	2.7	2.9	2.7	3.0	2.6	2.5	2.6	2.6	2.5	2.4	2.4	2.3	2.5	1.6	1.7
Saudi Arabia	2.8	3.7	3.4	2.6	2.4	2.4	2.3	2.4	2.3	2.3	2.5	2.4	2.4	2.6	2.5	2.5	2.4	2.6	2.9	2.8	2.5	2.4	2.7
Egypt	2.3	2.1	2.0	2.1	2.0	2.2	2.3	2.0	2.3	2.2	2.5	2.2	2.1	2.0	2.1	2.2	2.2	2.3	2.5	2.6	2.6	2.5	2.3
Mexico	0.8	1.8	1.9	1.8	1.8	2.0	2.2	2.3	2.2	2.2	1.9	2.0	1.9	1.8	2.0	2.0	2.1	2.3	2.4	2.4	2.3	2.2	2.3
Brazil	0.4	1.2	1.6	1.7	1.4	1.6	1.9	2.1	1.8	1.9	1.6	2.0	2.3	2.0	1.9	1.8	2.1	2.1	2.2	2.2	2.1	1.5	1.4
Venezuela	0.6	1.2	1.5	1.5	1.7	1.8	1.9	2.3	2.0	2.0	1.8	1.8	1.7	1.8	1.8	1.8	1.8	1.8	1.8	1.9	2.0	2.6	2.6
India	1.7	2.0	2.0	1.8	2.0	2.0	1.9	2.1	1.9	2.0	1.9	1.9	1.6	1.6	1.6	1.6	1.5	1.5	1.7	1.6	1.6	1.7	1.9
Angola		1.9	1.4	1.3	1.5	1.7	1.7	1.9	1.9	1.9	2.1	1.8	1.8	1.7	1.7	1.7	1.7	1.7	1.7	1.7	1.8	2.1	1.0
Canada	1.3	1.8	2.4	2.7	2.5	2.4	2.1	2.1	1.8	1.7	1.0	1.1	1.2	1.2	1.2	1.2	1.3	1.2	1.2	1.1	1.1	1.1	2.0
Oman	0.6	1.5	1.5	1.5	1.5	1.4	1.4	1.5	1.6	1.6	1.5	1.6	1.5	1.7	1.6	1.6	1.5	1.6	1.5	1.5	1.6	1.7	1.9
Qatar	0.9	0.8	0.8	0.8	0.9	1.1	1.7	1.5	1.7	1.5	1.7	1.6	1.7	1.9	1.6	1.8	1.8	1.7	1.6	1.6	1.4	1.4	0.9
Kuwait		1.4	1.5	1.5	1.4	1.3	1.3	1.3	1.2	1.4	1.7	1.5	1.4	1.5	1.6	1.5	1.5	1.6	1.5	1.4	1.3	1.2	0.8
Argentina	1.4	1.3	1.5	1.8	2.0	1.9	1.7	1.5	1.4	1.4	1.0	1.2	1.0	0.9	0.9	0.9	0.9	0.9	0.9	0.9	0.8	0.6	1.3
United Arab Emirates	2.1	1.7	1.5	1.5	1.5	1.5	1.3	1.2	1.4	1.2	1.1	1.0	1.0	0.9	1.0	1.0	1.1	0.9	1.0	1.1	1.1	1.2	1.0
Malaysia	0.7	0.7	0.7	0.8	0.8	0.8	1.0	0.8	1.0	1.0	0.9	1.3	1.2	1.3	1.3	1.3	1.5	1.4	1.4	1.4	1.5	1.5	1.2
Syria	1.8	1.5	1.4	1.5	1.5	1.5	1.4	1.3	1.2	1.4	1.6	1.3	1.0	0.9	0.9	0.8	0.8	0.9	0.9	1.0	0.9	0.5	0.6
Gabon	1.2	1.0	0.8	0.8	0.8	0.8	0.9	0.9	1.0	0.9	1.0	0.9	0.9	0.8	0.8	0.8	0.8	0.8	0.8	0.8	0.7	0.9	0.8
Australia	0.6	0.9	0.8	1.0	1.1	1.0	1.0	0.9	1.0	0.9	0.8	0.8	0.8	0.7	0.7	0.8	0.8	0.8	0.7	0.7	0.7	0.6	0.9
Ukraine	1.3	1.0	1.1	1.3	1.2	1.1	0.9	1.0	1.0	1.0	0.8	0.7	0.7	0.7	0.7	0.6	0.7	0.6	0.6	0.6	0.6	0.3	0.5
Turkmenistan	0.3	0.4	0.4	0.5	0.4	0.4	0.5	0.6	0.6	0.7	0.7	0.8	0.8	0.8	0.8	0.8	0.8	0.7	0.8	0.8	0.9	0.9	0.9

	1991	1992	1993	1994	1995	1996	1997	1998	1999	2000	2001	2002	2003	2004	2005	2006	2007	2008	2009	2010	2011	2012	2018
Russia				-0.3	0.1	0.3	-0.4	-1.1	0.6	-0.3	0.1	0.6	2.4	0.4	0.1	-0.1	-0.8	-0.5	-0.3	-1.0	-0.7		-5.0
Iran				-0.1	-0.3	-0.3	-0.4	-0.3	1.0	-0.7	0.9	-0.3	-0.3	-0.2	0.4	-0.0	-0.0	0.6	-0.1	-0.1	0.0		-1.3
Nigeria				-0.2	0.1	-0.3	-0.1	-0.2	0.1	-0.1	0.7	-0.5	-0.2	-0.4	-0.3	-0.4	-0.6	0.3	-0.3	0.4	0.1		-1.8
Algeria				-0.1	0.3	-0.5	-0.5	0.0	-0.7	0.6	0.3	-0.6	-0.2	0.1	-0.4	0.6	0.0	-0.2	-0.3	-0.1	0.2		-0.9
China				0.4	0.1	-0.1	0.1	-0.2	0.4	-0.0	-0.5	1.1	-0.9	0.5	0.4	0.0	0.1	-0.4	-0.1	-0.1	-0.1		-0.8
Iraq				0.0	-0.1	0.2	0.6	0.8	-0.0	0.6	0.7	-0.3	-0.3	0.1	-0.1	-0.1	0.2	0.2	0.4	0.2	0.3		-0.7
Libya				-0.3	-0.2	-0.0	-0.4	0.1	-0.4	0.3	0.3	-0.1	-0.2	-0.0	-0.1	0.1	-0.0	-0.2	-0.1	0.1	-0.3		-1.0
United States				0.2	0.1	-0.0	0.2	0.1	-0.1	-0.4	-0.8	0.1	0.3	-0.2	0.3	-0.0	-0.0	0.2	-0.0	0.5	1.1		14.2
Kazakhstan				-0.1	0.1	0.2	-0.0	0.0	-0.0	0.3	0.7	-0.2	0.2	0.3	-0.0	0.1	-0.1	-0.1	0.1	0.1	-0.2		-1.5
United Kingdom				0.2	-0.2	0.2	-0.3	0.2	-0.3	0.1	-0.5	-0.3	0.0	-0.3	-0.1	-0.1	0.2	-0.1	0.1	0.1	-0.3		-0.5
Indonesia				-0.0	-0.1	-0.6	0.7	-0.4	-0.1	0.1	-0.2	0.4	-0.4	-0.1	0.1	0.0	-0.1	-0.1	0.0	-0.2	0.2		-0.8
Saudi Arabia				-0.7	-0.2	-0.0	-0.1	0.1	-0.1	0.0	0.1	-0.0	-0.0	0.2	-0.1	-0.1	-0.0	0.2	0.3	-0.2	-0.2		0.2
Egypt				0.2	-0.1	0.1	0.1	-0.3	0.3	-0.1	0.3	-0.3	-0.1	-0.1	0.1	0.1	0.0	0.1	0.2	0.1	0.1		-0.4
Mexico				-0.1	-0.0	0.2	0.2	0.1	-0.1	0.0	-0.3	0.0	-0.1	-0.0	0.1	0.0	0.1	0.2	0.1	-0.0	-0.1		0.0
Brazil				0.1	-0.3	0.2	0.2	0.2	-0.2	0.0	-0.3	0.4	0.3	-0.3	-0.1	-0.1	0.2	0.1	0.1	-0.0	-0.1		-0.7
Venezuela				0.0	0.1	0.1	0.1	0.4	-0.2	0.0	-0.2	-0.0	-0.1	0.1	0.1	-0.0	-0.0	-0.0	0.0	0.0	0.1		0.6
India				-0.2	0.2	0.0	-0.1	0.2	-0.2	0.1	-0.1	-0.1	-0.2	-0.1	-0.0	-0.0	-0.0	-0.0	0.2	-0.0	-0.0		0.3
Angola				-0.1	0.2	0.2	0.0	0.2	-0.1	0.0	0.2	-0.3	-0.0	-0.1	0.0	-0.0	-0.0	0.0	-0.0	0.1	0.0		-0.8
Canada				0.3	-0.3	-0.1	-0.3	0.0	-0.3	-0.1	-0.7	0.1	0.1	0.0	-0.0	-0.1	0.1	-0.1	-0.0	-0.0	0.0		0.8
Oman				-0.0	0.0	-0.1	-0.1	0.1	0.1	-0.0	-0.1	0.1	-0.1	0.2	-0.1	-0.0	-0.1	0.0	-0.1	-0.0	0.2		0.3
Qatar				0.1	0.1	0.2	0.6	-0.2	0.3	-0.2	0.2	-0.2	0.2	0.1	-0.2	0.2	0.0	-0.1	-0.1	-0.0	-0.2		-0.6
Kuwait				-0.0	-0.1	-0.0	-0.0	0.0	-0.1	0.2	0.3	-0.2	-0.1	0.1	0.1	-0.2	0.1	0.1	-0.1	-0.2	-0.1		-0.5
Argentina				0.3	0.2	-0.1	-0.1	-0.2	-0.1	-0.1	-0.4	0.2	-0.2	-0.1	0.0	0.0	0.0	-0.1	0.1	-0.0	-0.1		0.4
United Arab Emirates				0.0	0.0	-0.0	-0.2	-0.1	0.1	-0.1	-0.1	-0.1	0.0	-0.1	0.0	0.0	0.1	-0.1	0.1	0.1	-0.0		-0.1
Malaysia				0.1	0.0	-0.0	0.2	-0.1	0.2	0.0	-0.2	0.4	-0.1	0.1	0.0	-0.0	0.2	-0.1	-0.0	-0.0	0.1		-0.3
Syria				0.1	-0.0	-0.1	-0.1	-0.0	-0.1	0.2	0.2	-0.3	-0.2	-0.1	-0.0	-0.1	-0.1	0.1	0.0	0.1	-0.1		-0.3
Gabon				0.0	-0.0	-0.0	0.1	-0.0	0.1	-0.2	0.1	-0.1	-0.0	-0.1	0.0	-0.0	0.0	-0.1	0.1	-0.0	-0.1		0.1
Australia				0.2	0.1	-0.0	-0.0	-0.1	0.1	-0.1	-0.1	0.0	-0.0	-0.1	0.0	0.0	0.0	0.0	-0.1	0.0	-0.1		0.3
Ukraine				0.2	-0.1	-0.1	-0.2	0.0	-0.0	0.1	-0.2	-0.2	0.1	-0.0	0.0	-0.1	0.1	-0.1	0.1	-0.0	-0.0		-0.1
Turkmenistan				0.1	-0.1	0.0	0.1	0.1	0.0	0.1	0.0	0.1	-0.0	-0.1	-0.0	0.1	0.0	-0.1	0.1	0.1	0.1		0.0

Fig. 7. This figure shows (a) annual total counts of 1-arcminute grid cells containing active industrial gas flares at a global scale from ATSR and SLSTR sensors, and (b) the various national proportions of this global figure. The national level reporting is carried out for the top 30 nations determined by summation across the reported proportions and that typically comprise ~95% of total FRP output from gas flaring. Shown in (c) are the annual changes in proportion between fully sampled years for each of the top 30 nations.

achieved as:

$$\overline{FRP} = \frac{\sum_{i}^{n} FRP}{S \bullet C} \quad (4)$$

where for a given grid cell and year $\overline{FRP}$ is the normalised FRP, n is the number of FRP observations, S the total number of overpasses and C the estimated fractional cloud cover [range: 0–1]. This approach normalises the FRP based on an estimated total number of cloud free overpasses (i.e. the total number of expected observations), thus removing bias associated with sampling and cloudiness. The calculation of the cloud cover and sampling for a grid cell was discussed in Section 2.5. A further issue is introduced through deficiencies in the ATSR-1 and SLSTR cloud masks, resulting in unrealistic global cloud fractions, as shown in Table 3. This would result in biases being introduced during the normalisation step, so to address this all ATSR-1 and SLSTR sites use the nearest AATSR and ATSR-2 grid cell cloud fraction mean for their normalisation (calculated from the entire grid cell time series), working under the assumption that for most regions worldwide no significant trend in mean annual cloud cover fraction has yet been observed (Stubenrauch et al., 2013). The updated annual mean cloud fraction values are also reported in Table 3, and are far more realistic than the ATSR-1 and SLSTR-derived values, all being close to 60%, as is expected for cloud fraction statistics derived from passive radiometers with which global fractions of between 60% and 70% are observed (Stubenrauch et al., 2013). The annual normalised FRPs are reasonably assumed to be representative of a given flare's radiant activity over a year and are summed globally to produce annual totals of flare radiant activity (Fig. 8a). The percentage contribution to the global annual radiant output for the top 30 flaring nations is shown in Fig. 8b, with the ranking determined by summing proportions across the available time series for a given nation. Annual changes in the share of the global proportion for each country and completely sampled year are shown in Fig. 8c, which highlights where substantial changes in the aggregated FRP statistic occurs. Considering all activity, the peak in radiant emissions occurs in the year 2000, with a global mean radiant output of ~15.1 GW. After 2000 a drop in output is observed to a minimum of ~13.1 GW in 2003, rising again to a peak of ~14.3 GW in 2006 before gradually declining to ~12.4 GW in 2011. However, recently this gradual reduction in output appears to have reversed, with a mean radiant output of ~13 GW observed by SLSTR over the 12-month period evaluated during 2017 and 2018. Russia historically flares the most gas, in particular between 2003 and 2007 where it contributed > 17% to the global radiant heat output of these years. However, it also shows the largest reduction in the proportion of radiant heat output with a ~4.5% decrease between the ATSR and SLSTR time series, placing it behind Iraq and Iran which both had large increases of > 3% over the same period, to ~16.5% and ~15.3% of global output respectively. Over the same period, the largest percentage increase in flare radiant heat output (~6.9%) occurs in Venezuela, taking its global share to ~10.4%. Despite the substantial (14.2%) increase in flare count in the United States between 2011 and 2018 shown in Section 4.1, the corresponding radiative heat output increase is limited to ~2.1% and for 2018 the observations over the United States comprise 2.9% of the global radiant heat total or ~0.38 GW. However, as shown in Section 3.2, the restrictions we are applying to the SLSTR sensor to ensure consistency with ATSR means that smaller flares or those operating more sporadically are not observed. We estimate that these missed flares may contribute up to 0.064 GW of additional annual output to the United States radiant heat total for SLSTR based on the product of the following figures: a total of 1569 missed flaring sites (obtained from differencing the (Liu et al., 2018) total of 3441 sites and the total we determine here from SLSTR of 1872) with an assumed cloud and sampling normalised annual FRP of 0.041 MW per site (calculated using Eq. (4) with an assumed annual summed FRP of 1.77 MW for each flare calculated from the VIIRS data used in Section 3.2 as the mean of all flares that are not seen by SLSTR (mean value of 0.31 MW) and mean number of observations for all flares over the United States in the SLSTR data record (n = 5.7). The assumed cloud and sampling normalisation factor of 43.4 is obtained from the SLSTR mean cloud cover and number of samples for all flare containing grid cells for the United States for the SLSTR data record assessed herein). This is an expected result as these flaring sites clearly have very short flare operating periods (< 60 days) associated with testing of extractive equipment before routine operation, intermittent maintenance and or repairs, or short-term periods of over pressurisation resulting in flare operation (Liu et al., 2018). Our analysis shows instead that a significant proportion of emissions come from a small subset of flaring locations (similar to the findings of Elvidge et al. (2015)), as can be seen in Fig. 9, which shows the cumulative percentage contribution of each flare to the total normalised FRP observed over the ATSR time series with 10% of all radiative emissions coming from just 88 (0.34%) of all flaring grid cells detected by ATSR. The most radiant flaring activities occur at the SH/DP CIS oil refinery located in the Hassi Messaoud oil field, Algeria [Lat: 31.67; Lon: 6.05], comprising ~0.95% of all emissions over the ATSR time series equivalent to ~26.5 GW.

4.3. DMSP flared gas estimates intercomparison and BCM estimates

In Elvidge et al. (2009) gas flaring estimates (in billions of m^3; BCM) obtained from the global gas flaring reduction (GGFR) partnership were compared to aggregated DMSP low light imaging digital counts for various active gas flare locations. Coefficients from the resulting linear regression were applied to global observations of digital counts associated with flaring activity to generate national-level annual statistics on flared gas volumes (in BCM). The DMSP time series used in Elvidge et al. (2009) runs from 1994 through 2008, coinciding with much of the ATSR period. In Elvidge et al. (2015) the DMSP BCM estimates have been shown to be highly correlated to BCM estimates derived from VIIRS NightFire for 2012, based on annual national-level FRP statistics generated similarly to those in Section 4.2. Here a more extensive calibration is made against the national level DMSP data from Elvidge et al. (2009) with the FRP data produced herein from ATSR (the same annual metric as used for the global statistics produced in Section 4.2, but aggregated nationally instead). Fig. 10 shows the result, based on yearly sampling for completely sampled ATSR years only. The pattern of data seen in Fig. 10 was fit using two different linear models, the first relating to annual data from Russia and Nigeria and the second for all other flaring countries. The need for the different models is assumed to be due to inadequacies in the DMSP product for Russia and Nigeria, with the output BCM values derived from the observed digital counts having a high bias, the potential causes of which are likely due to calibration issues from misreporting of flared gas quantities (Elvidge et al., 2009). Using the Fig. 10 relationship for all countries excluding Russia and Nigeria, total flared gas volumes are mapped across the ATSR time series in Fig. 11, and annual estimates are listed in Table 5. The values reported in Table 5 are consistent with those from Elvidge et al. (2015, 2009), as might be expected, but more significantly the coefficients derived in Fig. 10 can also be applied to the more recent SLSTR data to provide updated total flare gas volumes for the period 9th May 2017 through 8th May 2018. Here an estimated ~131 BCM of gas has been flared globally. The uncertainty on this estimate is difficult to ascertain as the errors introduced by the GGFR flare volume data used to calibrate the DMSP BCM estimates, and also the errors for the digital counts from DMSP, are unavailable. However, looking at specific data from the Nigerian National Petroleum Corporation, a total national flared volume of 8.14 BCM (287.59 billion cubic feet) was reported for 2017 (Nigerian National Petroluem Corporation, 2017), and applying the ATSR derived FRP-to-BCM coefficients (for all countries excluding Russia and Nigeria) to the SLSTR annual normalised FRP data for Nigeria we obtain a 12 month estimate of 8.49 BCM, providing an indication of the reasonableness of the global estimate obtained for SLSTR.

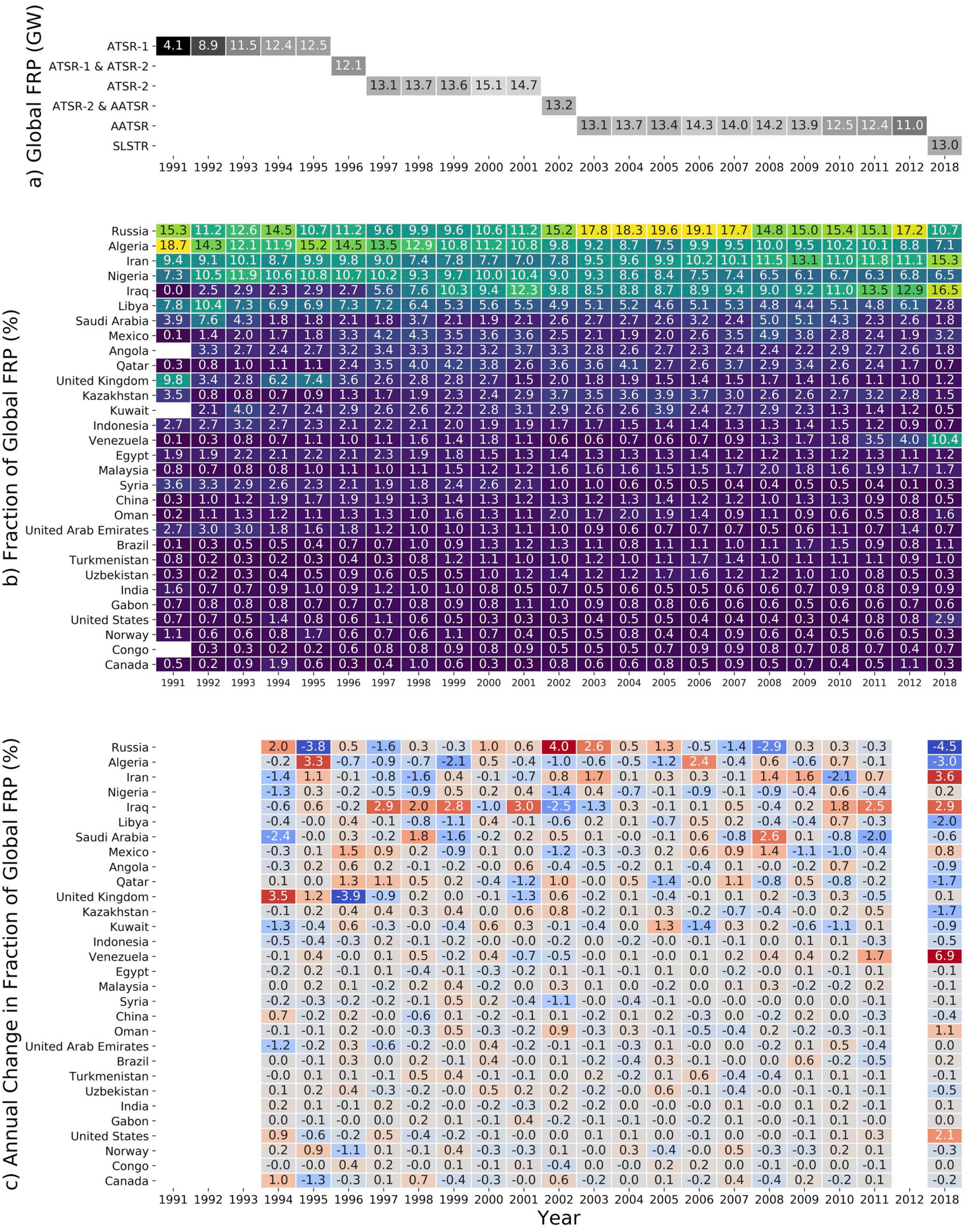

Fig. 8. Annual global cloud and sampling normalised FRP data for all flaring sites from the various sensors. (a) Global total, (b) national-level proportions of this global figure for the top 30 flaring nations (that typically comprise ~95% of total FRP output from gas flaring) determined by their overall total across the time series, (c) annual absolute change in proportion of the global gas flare FRP total for each nation (e.g. Russia experienced a 4.5% decrease in its proportion of global flaring activity in terms of FRP between 2011 and 2018, whilst Venezuela increased its contribution to the global total by 6.9% over the same period).

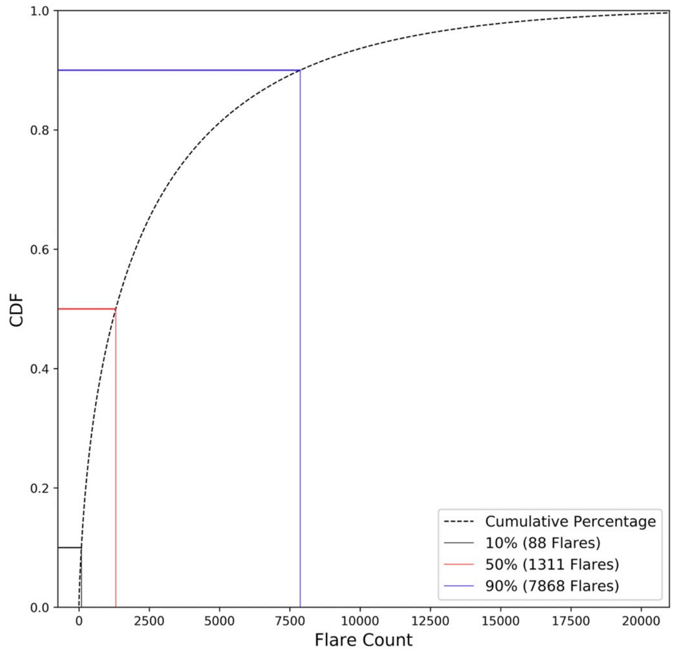

Fig. 9. The black dashed line in this figure shows the cumulative distribution function (CDF) of industrial gas flare FRP for all unique 1-arcminute flare associated grid cell for the ATSR time series. The solid black line indicates the number of 1-arcminute grid cells that produce 10% of the global FRP total for the ATSR time series, the solid red line indicates the number of grid cells that contain 50% of the global FRP total and the solid blue line the number of grid cells that contain 90% of the flaring activity. (For interpretation of the references to colour in this figure legend, the reader is referred to the web version of this article.)

4.4. Discussion

Of the two key indicators of gas flaring activity – total counts, and FRP-derived radiant power output statistics – assessed globally at annual intervals in Section 4.3, the FRP-based metric appears most useful as is it correlated with natural gas combustion rates as well as effectively representing the heterogeneity of gas flares in type and spatial density. The importance of this discrimination is especially apparent in the recent development of shale gas reserves (e.g. in the United States), which whilst being associated with substantial increases in flare counts are far less impactful in terms of increasing radiative output and flared gas volumes. At the other end of the spectrum, flaring counts in Venezuela have shown limited increases since 2011, yet flared gas volumes have grown substantially as indicated by our FRP based metric. Our main finding is that global gas flaring as expressed by annually flared volumes (in BCM) have not reduced between 2011 and 2017, and rather show a small (~5%) increase driven primarily by significant increases in Iraq, Iran and Venezuela that offset reductions in most other countries. Across the time series, various issues exist with data for ATSR-1 (1991 and 1992), ATSR-2 (2001 and 2002) and, in the case of ATSR-1, spurious observation are present in the Northern Hemisphere in 1994 and 1995. These introduce some biases into the generated FRP and BCM statistics, for example due to the incomplete sampling likely missing many of the smaller, more intermittent flares, and/or missing flaring activity due to seasonal illumination variation (e.g. the persistent illumination of high latitude Russian gas flaring sites during Northern Hemisphere summer) resulting in underestimated global totals as not all active flares are considered in the summations. Section 2.7 includes an attempt to remove the spuriously high FRP measures associated with ATSR-1 in the Northern Hemisphere during 1994 and 1995, and whilst it was successful in removing the more extreme events, it appears that some non-flaring activity not statistically separable from true flaring outputs remains. This result is evident in the FRP statistics generated for the United Kingdom and Norway (and also potentially Russia and Canada) where large oscillations in percentage point changes (Fig. 8c) between 1993 and 1996 are observed. However, excluding these nations for these years, reliable global- and national-level observations are available from 1993 through to 2018, providing the longest-term assessment of global-scale to country-scale gas flaring produced using satellite EO data to date. We have also produced the most recent estimate of global flared gas volume (~131 BCM) from the Sentinel-3 SLSTR sensor, first launched in February 2016.

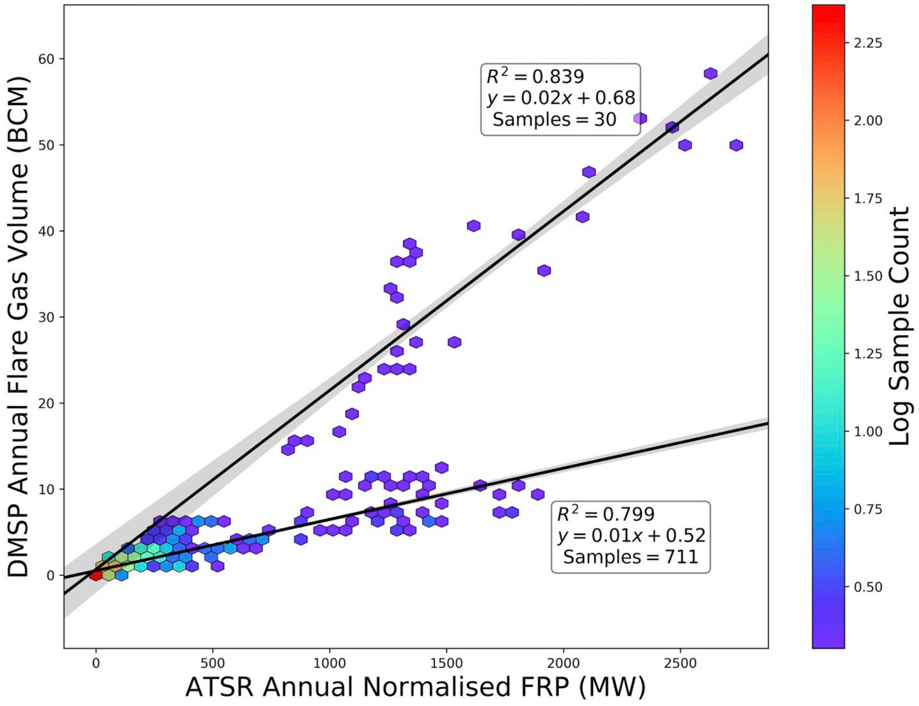

Fig. 10. Linear relationships between ATSR national level annual normalised gas flare FRP and the matching national level flare gas estimate (billions of cubic meters) derived from DMSP satellite observations. Two linear models are shown, one for Russian and Nigeria (30 sample points), and the other for all other gas flaring nations (711 sample points).

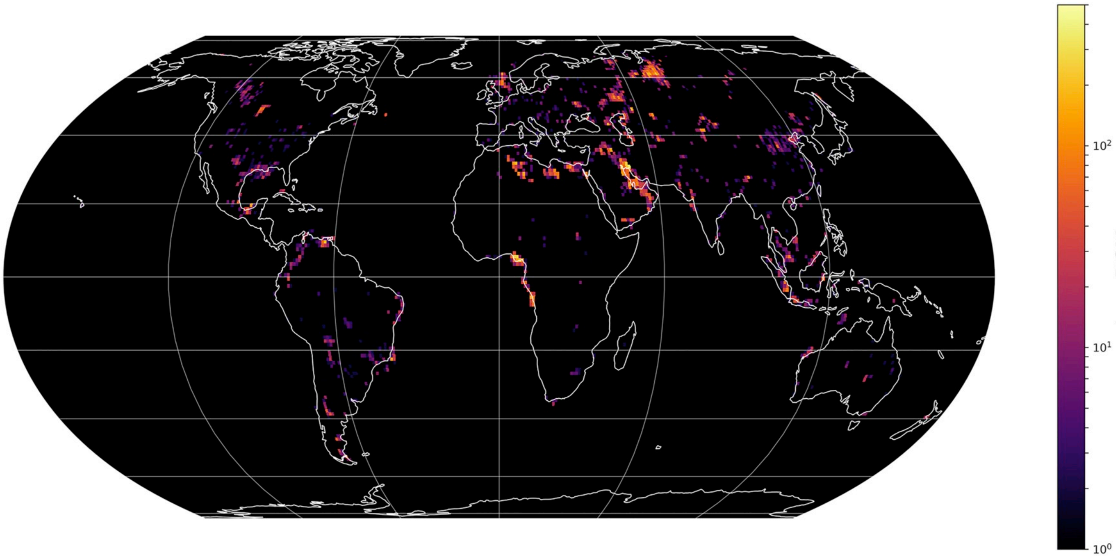

Fig. 11. Total flared gas volume (BCM) derived using the entire ATSR FRP time series for global gas flaring activity (binned into 1° resolution grid cells for display) and the linear models of Fig. 10.

5. Conclusions

We have produced the longest duration (1993 to 2018) annual inventory of industrial gas flaring activity at national to global scales using the ATSR and SLSTR series of spaceborne sensors, operating onboard the ERS, ENVISAT and Sentinel-3 series of European Earth Observation satellites. We report two key measures of flaring activity: annual counts of unique flaring sites; and annual totals of cloud cover and sampling normalised FRP. We conducted time series analyses for each of our gas flaring measures. Gas flare counts showed a general decreasing trend in the number of flaring sites for most nations, though an obvious exception is the United States, where a significant rise assumed to be associated with shale gas developments is observed. The United States now has the most industrial flaring sites worldwide, overtaking even Russia which had been the nation with most flaring sites since at least 1993. However, since our FRP-based inventorying metric is deemed to be correlated with gas flaring volumes, it is more effective at quantifying variations in the amounts of gas being flared than simple counts. Our most significant finding here is an apparent reversal in the reduction in global flaring activity observed in the ATSR time-series from 2003 up until 2011 (~5.5% decrease), with an increase of 4.8% (~0.6 GW) in our FRP-based statistic between 2011 and 2018. This increase is associated with substantial flaring enhancements in Venezuela, Iran and Iraq, increasing their share of the global total between 2011 and 2018 by ~6.9, ~3.6 and ~2.9% respectively, with decreasing shares observed over the same period in most other flaring nations, most notably Russia with an approximate 4.5% reduction in its share of the global total. The national level totals of our ATSR-derived FRP statistic were calibrated against DMSP-derived flare gas volume estimates in BCM and show a strong correlation ($R^2 \approx 0.8$) when considering all nations except Russia and Nigeria which lie on a different linear relation. When used with the SLSTR annual normalised FRP total, our relationship provide the most up-to-date estimate of global flaring gas volumes at ~131 BCM for the year between 9th May 2017 and 8th May 2018. Given the long-term funding commitment to the sentinel satellites as part of the EU Copernicus programme (Copernicus, 2017), continued inventorying of global gas flaring activity with Sentinel-3 SLSTR is possible until at least the 2030s, providing a tool for monitoring and evaluating the successes of gas flaring reduction initiatives and for targeting interventions.

The work herein represents the current state-of-the-art in the estimation of global flared gas volumes. However, it is based on calibrations to country-level reporting. It is likely that FRP-based measures can be used to directly estimate the rate of natural gas combustion using relations similar to those deployed to estimate vegetation fire biomass consumption (Wooster et al., 2005). Such relations will likely depend on gas composition; the flare combustion efficiency; and an appropriate technique to infer total flare FRP from the cross-sectional estimates currently provided by EO (Elvidge et al., 2015; Ismail and Umukoro, 2012; Zhang et al., 2015). Strides towards effectively solving the last of these issues have already been made (Elvidge et al., 2015; Zhang et al., 2015), and application of this overall approach would provide a remote sensing based technique for estimating flared gas volumes fully independent of nationally reported statistics.

Acknowledgments

VIIRS NightFire data were obtained via the NOAA National Centre for Environmental Information. VIIRS data were obtained via the NASA Level-1 and Atmosphere Archive and Distribution System. ATSR and SLSTR data were obtained via the Centre for Environmental Data Analysis archive. The authors were supported by funding from the Natural Environment Research Council (NERC) of the UK (PR140015 and NE/M017729/1). We thank the anonymous reviewers for their insightful comments and suggestions.

Table 5
Annual global flared gas estimates (BCM) from the ATSR and SLSTR sensors.

Year	'93	'94	'95	'96	'97	'98	'99	'00	'01	'02
BCM	115.3	124.9	125.6	121.5	131.5	137.8	137.0	151.7	147.9	132.9

Year	'03	'04	'05	'06	'07	'08	'09	'10	'11	'18
BCM	131.7	137.7	134.1	143.9	140.5	142.1	139.1	125.9	124.5	130.6

Appendix A. Supplementary data

Supplementary data to this article can be found online at https://doi.org/10.1016/j.rse.2019.111298.

References

Abuelgasim, A., Fraser, R., 2002. Day and night-time active fire detection over North America using NOAA-16 AVHRR data. In: Geoscience and Remote Sensing Symposium, 2002. IGARSS'02. 2002 IEEE International. IEEE, pp. 1489–1491.

Akpomuvie, O., 2011. Tragedy of commons: analysis of oil spillage, gas flaring and sustainable development of the Niger Delta of Nigeria. J. Sustain. Dev. 4, 200.

Anejionu, O.C.D., Blackburn, G.A., Whyatt, J.D., 2014. Satellite survey of gas flares: development and application of a Landsat-based technique in the Niger Delta. Int. J. Remote Sens. 35, 1900–1925.

Anejionu, O.C., Blackburn, G.A., Whyatt, J.D., 2015a. Detecting gas flares and estimating flaring volumes at individual flow stations using MODIS data. Remote Sens. Environ. 158, 81–94.

Anejionu, O.C., Whyatt, J.D., Blackburn, G.A., Price, C.S., 2015b. Contributions of gas flaring to a global air pollution hotspot: spatial and temporal variations, impacts and alleviation. Atmos. Environ. 118, 184–193.

Anenberg, S.C., Schwartz, J., Shindell, D., Amann, M., Faluvegi, G., Klimont, Z., Janssens-Maenhout, G., Pozzoli, L., Van Dingenen, R., Vignati, E., 2012. Global air quality and health co-benefits of mitigating near-term climate change through methane and black carbon emission controls. Environ. Health Perspect. 120, 831.

Bond, T.C., Doherty, S.J., Fahey, D.W., Forster, P.M., Berntsen, T., DeAngelo, B.J., Flanner, M.G., Ghan, S., Kärcher, B., Koch, D., 2013. Bounding the role of black carbon in the climate system: a scientific assessment. J. Geophys. Res. Atmos. 118, 5380–5552.

Burgi, P.-Y., Darrah, T.H., Tedesco, D., Eymold, W.K., 2014. Dynamics of the Mount Nyiragongo lava lake. J. Geophys. Res. Solid Earth 119, 4106–4122.

Calle, A., Casanova, J.-L., González-Alonso, F., 2009. Impact of point spread function of MSG-SEVIRI on active fire detection. Int. J. Remote Sens. 30, 4567–4579. https://doi.org/10.1080/01431160802609726.

Casadio, Arino, O., Serpe, D., 2012. Gas flaring monitoring from space using the ATSR instrument series. Remote Sens. Environ. 116, 239–249.

Chowdhury, S., Shipman, T., Chao, D., Elvidge, C.D., Zhizhin, M., Hsu, F.-C., 2014. Daytime gas flare detection using Landsat-8 multispectral data. In: Geoscience and Remote Sensing Symposium (IGARSS), 2014 IEEE International. IEEE, pp. 258–261.

Copernicus, 2017. Copernicus in Brief | Copernicus [WWW Document]. URL. https://www.copernicus.eu/en/about-copernicus/copernicus-brief, Accessed date: 18 January 2019.

Croft, T.A., 1973. Burning waste gas in oil fields. Nature 245, 375.

Denis, M.-A., Muller, J.-P., Mannstein, H., 2007. ATSR-2 camera models for the automated stereo photogrammetric retrieval of cloud-top heights—initial assessments. Int. J. Remote Sens. 28, 1939–1955. https://doi.org/10.1080/01431160600641723.

Doherty, S.J., Warren, S.G., Grenfell, T.C., Clarke, A.D., Brandt, R.E., 2010. Light-absorbing impurities in Arctic snow. Atmos. Chem. Phys. 10, 11647–11680.

Elvidge, C.D., Ziskin, D., Baugh, K.E., Tuttle, B.T., Ghosh, T., Pack, D.W., Erwin, E.H., Zhizhin, M., 2009. A fifteen year record of global natural gas flaring derived from satellite data. Energies 2, 595–622.

Elvidge, C.D., Zhizhin, M., Hsu, F.-C., Baugh, K.E., 2013. VIIRS nightfire: satellite pyrometry at night. Remote Sens. 5, 4423–4449.

Elvidge, C.D., Zhizhin, M., Baugh, K., Hsu, F.-C., Ghosh, T., 2015. Methods for global survey of natural gas flaring from visible infrared imaging radiometer suite data. Energies 9, 14.

Elvidge, C.D., Bazilian, M.D., Zhizhin, M., Ghosh, T., Baugh, K., Hsu, F.-C., 2018. The potential role of natural gas flaring in meeting greenhouse gas mitigation targets. Energy Strateg. Rev. 20, 156–162. https://doi.org/10.1016/j.esr.2017.12.012.

Faruolo, M., Coviello, I., Filizzola, C., Lacava, T., Pergola, N., Tramutoli, V., 2014. A satellite-based analysis of the Val d'Agri Oil Center (southern Italy) gas flaring emissions. Nat. Hazards Earth Syst. Sci. 14, 2783–2793. https://doi.org/10.5194/nhess-14-2783-2014.

Faruolo, M., Lacava, T., Pergola, N., Tramutoli, V., 2018. On the potential of the RST-FLARE algorithm for gas flaring characterization from space. Sensors (Basel) 18. https://doi.org/10.3390/s18082466.

Fawole, O.G., Cai, X.-M., MacKenzie, A.R., 2016. Gas flaring and resultant air pollution: a review focusing on black carbon. Environ. Pollut. 216, 182–197.

Fisher, D., Wooster, M.J., 2018. Shortwave IR adaption of the mid-infrared radiance method of fire radiative power (FRP) retrieval for assessing industrial gas flaring output. Remote Sens. 10, 305.

Flanner, M.G., Zender, C.S., Randerson, J.T., Rasch, P.J., 2007. Present-day climate forcing and response from black carbon in snow. J. Geophys. Res. Atmos. 112.

Giglio, L., Schroeder, W., Justice, C.O., 2016. The collection 6 MODIS active fire detection algorithm and fire products. Remote Sens. Environ. 178, 31–41.

Global Volcanism Program, 2013. In: Venzke, E. (Ed.), Volcanoes of the World, v. 4.7.5. Smithsonian Institution. https://doi.org/10.5479/si.GVP.VOTW4-2013. Downloaded 18 Jan 2019.

Hadley, O.L., Kirchstetter, T.W., 2012. Black-carbon reduction of snow albedo. Nat. Clim. Chang. 2, 437.

Highwood, E.J., Kinnersley, R.P., 2006. When smoke gets in our eyes: the multiple impacts of atmospheric black carbon on climate, air quality and health. Environ. Int. 32, 560–566.

Huang, K., Fu, J.S., Prikhodko, V.Y., Storey, J.M., Romanov, A., Hodson, E.L., Cresko, J., Morozova, I., Ignatieva, Y., Cabaniss, J., 2015. Russian anthropogenic black carbon: emission reconstruction and Arctic black carbon simulation. J. Geophys. Res. Atmos. 120.

Ismail, O.S., Umukoro, G.E., 2012. Global impact of gas flaring. Energy Power Eng. 4, 290–302. https://doi.org/10.4236/epe.2012.44039.

Janssen, N.A., Gerlofs-Nijland, M.E., Lanki, T., Salonen, R.O., Cassee, F., Hoek, G., Fischer, P., Brunekreef, B., Krzyzanowski, M., 2012. Health Effects of Black Carbon. WHO Regional Office for Europe Copenhagen.

Leifer, I., Lehr, W.J., Simecek-Beatty, D., Bradley, E., Clark, R., Dennison, P., Hu, Y., Matheson, S., Jones, C.E., Holt, B., 2012. State of the art satellite and airborne marine oil spill remote sensing: application to the BP Deepwater Horizon oil spill. Remote Sens. Environ. 124, 185–209.

Liu, Y., Hu, C., Zhan, W., Sun, C., Murch, B., Ma, L., 2018. Identifying industrial heat sources using time-series of the VIIRS Nightfire product with an object-oriented approach. Remote Sens. Environ. 204, 347–365. https://doi.org/10.1016/j.rse.2017.10.019.

Marine Regions, 2018. Marine Regions [WWW Document]. http://marineregions.org/, Accessed date: 11 July 2018.

Muirhead, K., Cracknell, A.P., 1984. Identification of gas flares in the North Sea using satellite data. Int. J. Remote Sens. 5, 199–212.

Nigerian National Petroluem Corporation, 2017. NNPC Monthly Financial Operations Report for the Month of December 2017.

Prata, A.J.F., Cechet, R.P., Barton, I.J., Llewellyn-Jones, D.T., 1990. The along track scanning radiometer for ERS-1-scan geometry and data simulation. IEEE Trans. Geosci. Remote Sens. 28, 3–13. https://doi.org/10.1109/36.45741.

Ramanathan, V., Carmichael, G., 2008. Global and regional climate changes due to black carbon. Nat. Geosci. 1, 221.

Reed, R.J., 1986. Combustion Handbook. I North American Mfg. Co., Cleveland, OH.

Roberts, G.J., Wooster, M.J., 2008. Fire detection and fire characterization over Africa using Meteosat SEVIRI. IEEE Trans. Geosci. Remote Sens. 46, 1200–1218.

Schroeder, W., Oliva, P., Giglio, L., Csiszar, I.A., 2014. The new VIIRS 375 m active fire detection data product: algorithm description and initial assessment. Remote Sens. Environ. 143, 85–96.

Schroeder, W., Oliva, P., Giglio, L., Quayle, B., Lorenz, E., Morelli, F., 2016. Active fire detection using Landsat-8/OLI data. Remote Sens. Environ. 185, 210–220.

Serreze, M.C., Barry, R.G., 2011. Processes and impacts of Arctic amplification: a research synthesis. Glob. Planet. Chang. 77, 85–96.

Smith, D., 2018. Sentinel-3 SLSTR – Performance and Calibration. Sentinel-3 Validation Team Meeting.

Smith, D.L., Cox, C.V., 2013. (A) ATSR solar channel on-orbit radiometric calibration. IEEE Trans. Geosci. Remote Sens. 51, 1370–1382.

Smith, D., Mutlow, C., Delderfield, J., Watkins, B., Mason, G., 2012. ATSR infrared radiometric calibration and in-orbit performance. Remote Sens. Environ. 116, 4–16.

Stohl, A., Klimont, Z., Eckhardt, S., Kupiainen, K., Shevchenko, V.P., Kopeikin, V.M., Novigatsky, A.N., 2013. Black carbon in the Arctic: the underestimated role of gas flaring and residential combustion emissions. Atmos. Chem. Phys. 13, 8833–8855.

Stubenrauch, C.J., Rossow, W.B., Kinne, S., Ackerman, S., Cesana, G., Chepfer, H., Di Girolamo, L., Getzewich, B., Guignard, A., Heidinger, A., 2013. Assessment of global cloud datasets from satellites: project and database initiated by the GEWEX radiation panel. Bull. Am. Meteorol. Soc. 94, 1031–1049.

The World Bank, 2011. Global Gas Flaring Reduction Partnership: Improving Energy Efficiency & Mitigating Impact on Climate Change [WWW Document]. World Bank. http://siteresources.worldbank.org/INTGGFR/Resources/GGFR_NewBrochure%28Oct2011%29.pdf, Accessed date: 22 June 2018.

The World Bank, 2015. Zero Routine Flaring by 2030 [WWW Document]. World Bank URL. http://www.worldbank.org/en/programs/zero-routine-flaring-by-2030, Accessed date: 22 June 2018.

Wooster, M.J., Rothery, D.A., 1997. Thermal monitoring of Lascar Volcano, Chile, using infrared data from the along-track scanning radiometer: a 1992–1995 time series. Bull. Volcanol. 58, 566–579.

Wooster, M.J., Rothery, D.A., 2002. A review of volcano surveillance applications using the ATSR instrument series. Adv. Environ. Monit. Model. 1, 97–123.

Wooster, M.J., Rothery, D.A., Sear, C.B., Carlton, R.W.T., 1998. Monitoring the development of active lava domes using data from the ERS-1 along track scanning radiometer. Adv. Space Res. 21, 501–505.

Wooster, M.J., Zhukov, B., Oertel, D., 2003. Fire radiative energy for quantitative study of biomass burning: derivation from the BIRD experimental satellite and comparison to MODIS fire products. Remote Sens. Environ. 86, 83–107.

Wooster, M.J., Roberts, G., Perry, G.L.W., Kaufman, Y.J., 2005. Retrieval of biomass combustion rates and totals from fire radiative power observations: FRP derivation and calibration relationships between biomass consumption and fire radiative energy release. J. Geophys. Res. Atmos. 110.

Wooster, M.J., Xu, W., Nightingale, T., 2012. Sentinel-3 SLSTR active fire detection and FRP product: pre-launch algorithm development and performance evaluation using MODIS and ASTER datasets. Remote Sens. Environ. 120, 236–254.

Wooster, M.J., Roberts, G., Freeborn, P.H., Xu, W., Govaerts, Y., Beeby, R., He, J., Lattanzio, A., Fisher, D., Mullen, R., 2015. LSA SAF Meteosat FRP products–part 1: algorithms, product contents, and analysis. Atmos. Chem. Phys. 15, 13217.

Zhang, X., Kondragunta, S., Roy, D.P., 2014. Interannual variation in biomass burning and fire seasonality derived from geostationary satellite data across the contiguous United States from 1995 to 2011. J. Geophys. Res. Biogeosci. 119, 1147–1162. https://doi.org/10.1002/2013JG002518.

Zhang, X., Scheving, B., Shoghli, B., Zygarlicke, C., Wocken, C., 2015. Quantifying gas flaring CH4 consumption using VIIRS. Remote Sens. 7, 9529–9541.

Zhang, T., Wooster, M.J., Xu, W., 2017. Approaches for synergistically exploiting VIIRS I- and M-Band data in regional active fire detection and FRP assessment: a demonstration with respect to agricultural residue burning in Eastern China. Remote Sens. Environ. 198, 407–424.